ALMA MATER STUDIORUM
UNIVERSITÀ DI BOLOGNA

Scuola di Ingegneria

Corso di Laurea in

Ingegneria Elettronica e Telecomunicazioni per l'Energia

DESIGN AND ANALYSIS OF OPTICAL LINKS FOR SPACE COMMUNICATIONS

Elaborato in

Teoria dell'Informazione e Crittografia LM

Tesi di Laurea di:
ALBERTO FAEDI

Relatore:
Chiar.mo Prof. Ing.
MARCO CHIANI

Correlatori:
Prof. Ing.
ENRICO PAOLINI
Ing.
LORENZO VALENTINI

SESSIONE III

ANNO ACCADEMICO 2019–2020

KEY WORDS

Iterative Decoding

SCPPM

LDPC

Link Budget

Deep-Space

Contents

Introduction

Over the past few years, there has been a growing interest in communication systems based on free space optical (FSO) transmissions. One of the reasons for this interest is the increased amount of data generated by scientific deep-space missions, whose communication involves satellites in orbit around planets. The transition from radio frequency (RF) bands to the optical ones has the potential to allow an increment of data rate. Besides that, the interest of establishing a communication link for satellites located at a long distance from the Earth is also a purpose for the development of the optical technology.
Of course, RF systems constitute a consolidated and reliable solution for space communication, because of the many years of testing, missions and achievements. However, optical frequencies can provide improvements under various aspects.

The main advantage is related to the use of small wavelength. In fact, beams emitted from finite-width antennas spread-out in space: as the distance from the transmitting system increases, the signal power is distributed over an increasingly bigger area. For directive antennas, the angular beamwidth scales generally as

$$\Theta \propto \frac{\lambda}{D} \tag{1}$$

where λ is the carrier wavelength, and D is the aperture diameter of the transmitting antenna. The definition of Θ can be, e.g., the angular distance between the first minimum next to the main lobe of the antenna pattern,

and the maximum of the main lobe itself.
Choosing a wavelength smaller than the ones at RF, means reducing the effect of beam divergence. Therefore, with optical frequencies it is possible, for given antenna dimensions, to concentrate the power of the beam in a smaller area, or, equally, to supply the same power density in a longer distance between transmitting and receiving antennas, because of the smaller divergence. The resulting advantage in the link budget gives rise to a potential higher data rate.
The difference between the RF and optical wavelength is 3 to 5 orders of magnitude, because the shift of frequencies goes from hundreds of GHz, to hundreds of THz. For this reason, the value of λ in equation (1) reduces Θ so much that a decrease of the antenna dimension does not overcome the previous benefit. Therefore, with optical frequencies, it is possible to reduce mass, dimensions, and costs of the transmitting and receiving satellites. This reduction also applies for receiving antennas, because of the narrow beam divergence. However, if the antenna is very directive, the pointing requirements will be very challenging. A miss-pointing error in optical frequencies can lead to a remarkable loss in received power. This is one of the bigger optical link drawbacks.

Another problem with optical communication is the beam attenuation in atmosphere. Optical wavelengths are more affected from atmospheric channel effects than RF ones. Effects like absorption, scattering and turbulence are critical for optical transmission because of the smaller wavelength. However, several missions, testing optical communication, have been developed. NASA's Mars laser communications demonstration (MLCD), NASA's lunar laser communications demonstration (LLCD), and optical payload for lasercomm science (OPALS), developed at Jet Propulsion Laboratory, are examples of links between a satellite or a spacecraft in orbit around Earth and a terrestrial receiver. The main goal of these missions is the development of the new technology, trying to achieve faster data rate, as mentioned before. It is also interesting to implement optical links in free-space between satellites, like, for example, ESA's semiconductor-laser intersatellite

link experiment (SILEX) or ESA's european data relay satellite (EDRS). In particular, the latter project consists in a constellation of geosynchronous equatorial orbit (GEO) satellites relay, that exchange data from other systems in space to Earth receivers. The idea of space data relaying has been known for a long time, being first pictured by NASA. In 1983, the first ever tracking and data relay satellite (TDRS) became operational, with the aim of providing near continuous communications and tracking services to low-Earth orbit (LEO) spacecrafts, launch vehicles, and suborbital platforms in general. The concept behind those project has also been applied to the two-leg deep-space (2-LDS) relay system, a project that aims at investigating the feasibility and the performance of a 2-leg architecture. The link between the deep-space satellites and the relay satellite might take advantage of the optical band because of the absence of the atmosphere, and it might be able to overcome the huge distance between Earth and other planets like Neptune or Uranus. The 2-LDS project is aimed to examine if the double link, one of them being optical, can achieve better performance than the direct Earth-satellite one.

In Fig. 1 is shown a graphical representation of optical communication links, summarizing the previous information: the red bidirectional arrows and the red and white unidirectional arrows represent optical links between spacecrafts and Earth receivers or transmitters; instead, the dotted arrows represent optical communication links between spacecrafts.

This thesis will study and simulate two different modulation and demodulation techniques in relation to the optical leg of the previously described architecture. Chapter 1 will show some concepts related to the optical channel, its description, and the related losses. In chapter 2 the serially concatenated pulse-position modulation (SCPPM) system will be explained, describing the encoder and modulation sub-system, and successively a possible decoding implementation. In chapter 3 the link budget performances will be described, while in chapter 4 the LDPC modulation and demodulation method will be explained.

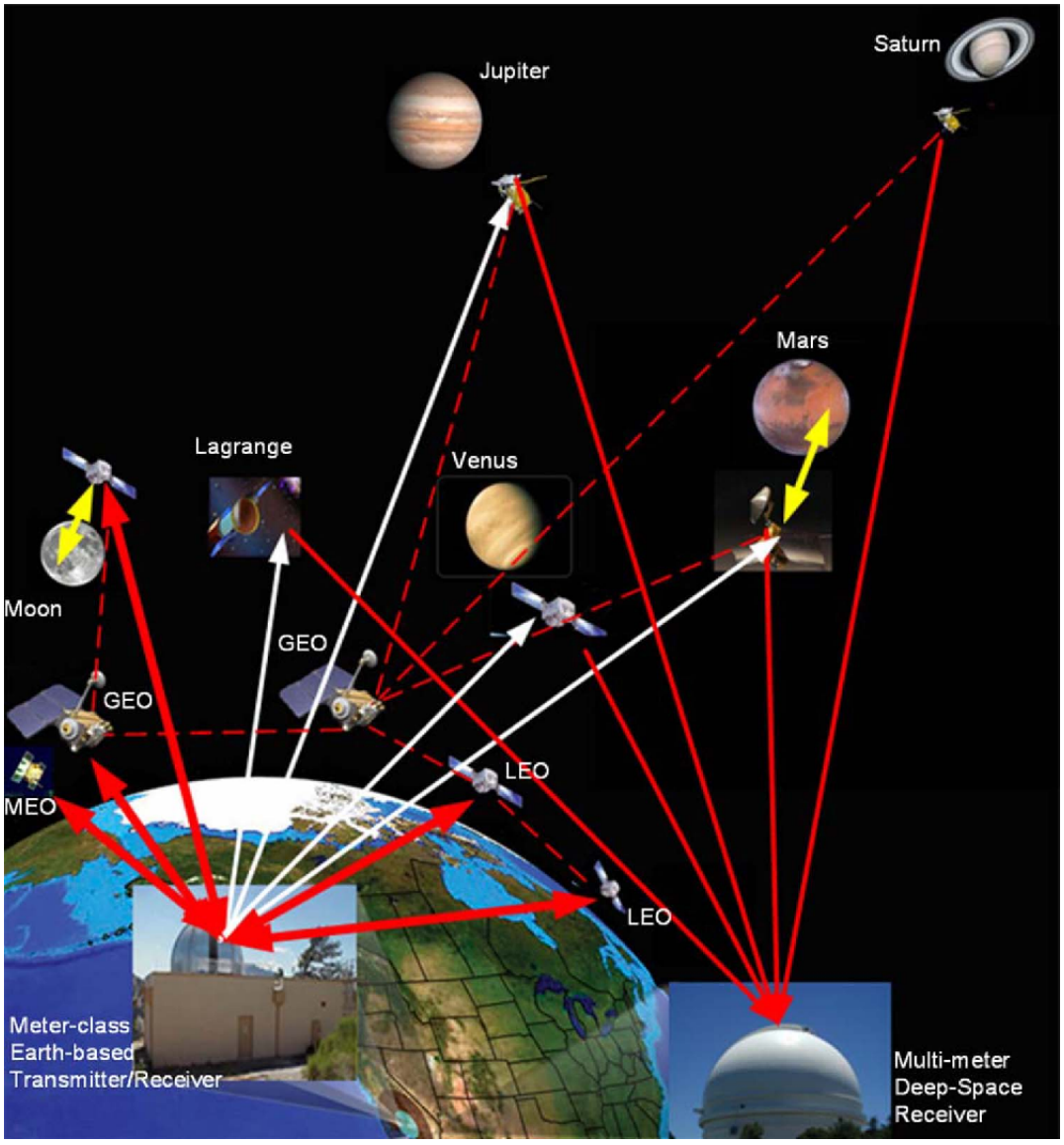

Figure 1: Graphical representation of optical communication links [1].

Chapter 1

Deep-Space Optical Communications

In this chapter a general overview of the deep-space optical links and communications is described. All these information will be useful for the comprehension of the concepts of the next chapters. In the following paragraphs, the optical channel model is described, along with the technological systems that have been investigated for the modulation and demodulation process, and for the link budget evaluation. Moreover, all the losses involved in the overall system are described.

1.1 PPM Modulation on Poisson Channels

In order to determine how the information travels from the transmitting to the receiving antennas, it is first necessary to describe the channel model. Its description derives from the modulation and coding technique used to transmit data information, and from the technology used to send and receive the signal.
As it will be better explained in chapter 2, data bits are modulated using the modulation technique named pulse-position modulation (PPM): the frame sent into the channel is a sequence of laser pulses, for which a slot without a pulse identifies a '0', while an impulse identifies a '1'. For the peak and

average power constraints typical of a deep-space link, restricting the modulation to PPM is near-capacity achieving [2].
Therefore, the receiver must detect the transmitted optical impulses. The technology used to perform this task is not unique and different implementations lead to different mathematical model descriptions.

Let us assume a photon counting device, such as a photomultiplier tube (see section 1.2.4), in addition to the PPM modulation. The output of such a device, for a certain time interval, is the number of photons observed. The resulting channel model is described by the Poisson process.

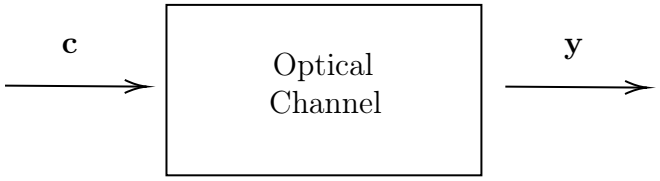

Figure 1.1: Conceptual scheme of the optical channel

As Fig. 1.1 shows, the optical channel can be represented conceptually by a block that takes as input a sequence $\mathbf{c} = (\mathbf{c}_0, \mathbf{c}_1, \ldots, \mathbf{c}_{S-1})$ and generates a sequence $\mathbf{y} = \big(\mathbf{y}_0, \mathbf{y}_1, \ldots, \mathbf{y}_{S-1}\big)$. Each $\mathbf{c}_i$ represents a PPM symbol composed by $M-1$ slots without laser pulse and one with a laser pulse, while S is the number of PPM symbols in a transmitted frame.
The sequence $\mathbf{y}$ derives from the channel statistics and each value of $\mathbf{y}_i = \big(y_i^0, y_i^1, \ldots, y_i^{M-1}\big)$ can be modeled as a memoryless time-invariant Poisson process with conditional probability mass function (pmf) [2, 3].

$$\begin{aligned} p_1\left(y_i^q\right) &\triangleq \mathbb{P}\{y_i^q \,|\, c_i^q = 1\} = \frac{\left(n_\mathrm{s} + n_\mathrm{b}\right)^{y_i^q}}{y_i^q!}\, e^{-(n_\mathrm{s}+n_\mathrm{b})} \\ p_0\left(y_i^q\right) &\triangleq \mathbb{P}\{y_i^q \,|\, c_i^q = 0\} = \frac{n_\mathrm{b}^{y_i^q}}{y_i^q!}\, e^{-n_\mathrm{b}} \end{aligned} \tag{1.1}$$

Here, M is the PPM order, i.e., the number of slots in a PPM symbol, n_s is the mean number of signal photons per slot, n_b is the mean number of noise photons per slot, and q is an index that goes from 0 to $M-1$ represent-

ing the q-th PPM slot; y_i^q identifies a random variable given by a Poisson distribution with mean parameter $n_\mathrm{s} + n_\mathrm{b}$ or n_b, in a signal slot and in a noise slot, respectively. Therefore, equations (1.1) represent the probability that y_i^q photons have been detected when it has been transmitted or not an impulse.

From these statistics, it is possible to calculate the likelihood ratios at the channel output. This information will be necessary in the algorithm for the decoding of the received signal. The whole algorithm will be explained in details in chapter 2. Considering a single PPM slot, the likelihood ratio is defined as

$$L\left(y_i^q\right) \triangleq \frac{p_0\left(y_i^q\right)}{p_1\left(y_i^q\right)} = \left(\frac{n_\mathrm{b}}{n_\mathrm{s} + n_\mathrm{b}}\right)^{y_i^q} e^{n_\mathrm{s}}\,. \tag{1.2}$$

Equation (1.2) derives from detection and estimation theory: if the computed value is greater than 1, it is more likely that the obtained y_i^q photons are due to a 0 transmission; if the computed value is smaller than 1, instead, it is more likely that it has been transmitted an impulse. Equation (1.2) can be given in a logarithmic form; in this case it is named log-likelihood ratio (LLR), and the decision threshold is at 0 (that is the logarithmic value of (1.2) when $p_0\left(y_i^q\right) = p_1\left(y_i^q\right)$).
The decoding algorithm needs a log-likelihood description for every single PPM symbol received and detected. When $n_\mathrm{b} > 0$, the channel log-likelihoods for the symbols are

$$\begin{aligned} \overline{\pi}\left(\mathbf{c}_i^j\right) &= \log p\left(\mathbf{y}_i \,|\, \mathbf{c}_i^j\right) \\ &= \log \frac{p_0\left(y_i^j\right)}{p_1\left(y_i^j\right)} + \mathcal{C} \\ &= y_i^j \log\left(1 + \frac{n_\mathrm{s}}{n_\mathrm{b}}\right) + \mathcal{C}\,. \end{aligned} \tag{1.3}$$

Iterative decoding algorithm requires likelihoods to be computed for every slot of each PPM symbol of the transmitted codeword. $\mathcal{C}$ is a constant that

includes all the remaining probability $p_0(y_i^q)$ calculated supposing an empty slot for each $q \neq j$. Finally, $\mathbf{c}_i^j$ represents the hypothesis that the PPM symbol has an impulse in the j-th slot.

The PPM channel capacity descends from all of those considerations, as described in [4]. The capacity of M-ary PPM on a soft-output channel is shown to be

$$C(M) = \frac{1}{M} E_{Y_1,\ldots,Y_M} \log_2 \left[\frac{ML(Y_1)}{\sum_{j=1}^{M} L(Y_j)} \right], \text{ bit/slot} \tag{1.4}$$

where Y_1 has distribution $p_1(\cdot)$, Y_j has distribution $p_0(\cdot)$ for all $j > 1$, and $L(y)$ is the likelihood ratio described in equation (1.2).

1.2 System Technology

Spacecraft and satellites relays, in orbit or in deep-space, require many developed subsystems and technologies. Each part of the entire system is fundamental for the regular functioning, that it has to be the more enduring as possible. Along the years and the missions accomplished, a lot of improvements have been achieved [5].
As regards the optical communications, the most significant parts of the spacecraft are the laser transmitter, the antenna, the pointing system, and the detector.

In Fig. 1.2 is shown one of the modules used in the LLCD NASA demonstration. It is possible to see the optical unit with the laser antenna, assembled on the side of the structure, trying not to cover the solar panel arranged around it. Moreover, on the inside of the module there are the modulation-demodulation device and the controller device, the former required for the transmitting and receiving signals processing.

In Fig. 1.3, instead, is shown the particular transmitting and receiving laser unit assembled in a EDRS relay satellite by ESA. The laser is placed

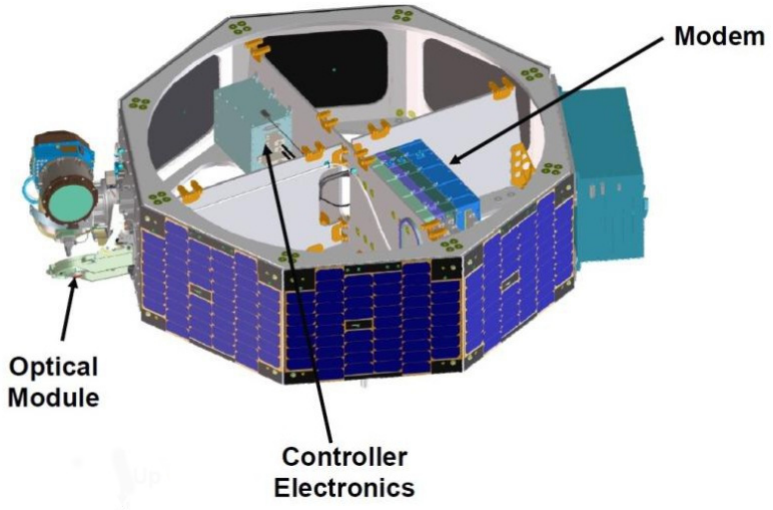

Figure 1.2: Graphic representation of the LLCD module.

onto a double rotational machinery, electrically and mechanically controlled; this aims to the correct beam pointing towards others receiving and transmitting optical systems.

1.2.1 Laser Transmitters

Lasers transmitters must provide for an high quality optical beam, along with a specific average and peak output power, good efficiencies, reliability, and preferably with a limited weight and small size. Moreover, lasers must be able to produce an high variable impulsed optical power for signal modulation.

Many improvements have been done for the laser transmitters since the beginning of optical communications. Early transmitters had limited power (hundreds of mW) and very low efficiencies. Between them, the wall-plug efficiency has been very critical: this is because of the fact that in deep-space missions the power generation presents a very high level of difficulty, so it is essential to waste as little power as possible. Levels between 8 to 10 percent of wall-plug efficiency are considered reasonable, as described for a Mars

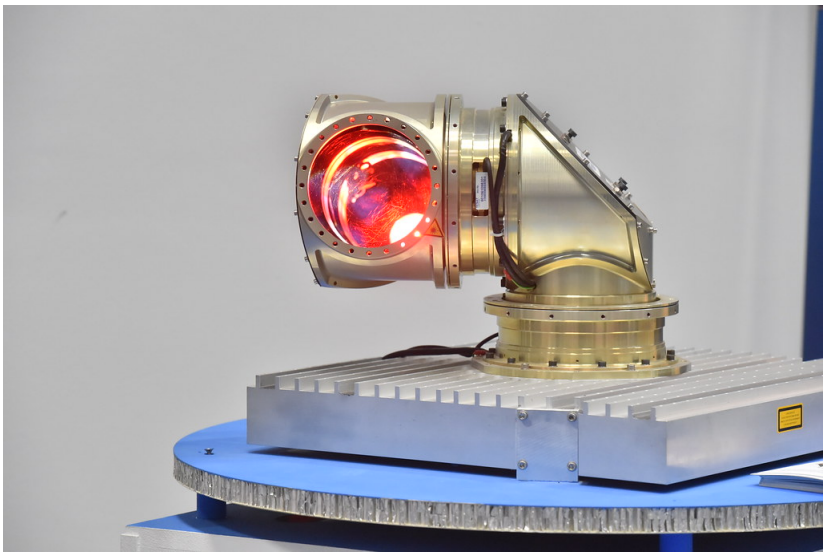

Figure 1.3: Optical laser unit, in a EDRS satellite relay.

downlink budget in [6].
At the beginning of the laser transmitter studies, semiconductor laser were tested. Today, viable technologies for deep-space mission are solid-state lasers, where the most common is the Nd:YAG type, or fiber-amplified lasers. They are able to provide high peak power along with moderate average power [5].

PPM modulation requires that the laser energy be concentrated in high peak pulses. However, laser transmitters have constraints in peak and average power imposed by physical limitations and available resources. The mean power is obtained by averaging the peak power for each M slots in a PPM symbol, also considering the time of laser recharge.

Laser wavelength is a fundamental choice in the project design phase. This decision has interest in and is influenced by many aspects of the link. First of all, the antenna gain is inversely proportional to the square of the wavelength; link performances are enhanced with a shorter wavelength, because of the narrower beam that concentrate transmitted energy in a smaller area. At the same time, it is easier to keep a good pointing angle between

	Yb YAG 1030 nm	Nd YVO4 1064 nm	Yb Fiber 1080 nm	Yb/Er Fiber 1550 nm	Er Fiber 1560 nm	Er Fiber 1570 nm	Er Fiber 1590 nm	Er YAG 1645 nm	Tm Fiber 2095 nm	Comment
Net gain dB (ph/m²/W)–atmos. attn., dB	308	306	307	305	302	304	305	301	306	Efficiency of delivering photons/unit transmitter area/W of S/C DC power
Additive bkgrnd noise dB–(ph/m²)	67	67	67	62	62	62	62	62	58	Additive noise reduces channel throughput
Peak-to-average ratio at high average power	Yes	Ltd avg power	Yes	Yes	TBD	TBD	TBD	Yes	Yes	High average power and high peak-to-average power ratio
PC detection efficiency, %	30–60	30–60	30–60	30–60	30–60	30–60	30–60	TBD	TBD	Link performance
Laser TRL	4	9*	5	5	4	4	4	4	4	Technology development required
Transmit/recv isolation										Eases the optical design of the flight transceiver
Total score	9	8	10	11	8	8	8	7	8	Green 2, Yellow 1, Red 0

Figure 1.4: Downlink wavelength trade summary [6].

the transmitting and receiving antennas with longer wavelength, because of the inverse proportionality between frequency and the laser beam-width, as described in equation (1).

Laser wavelength must also be selected in relation to the power constraints, efficiencies, isolation, and background noise of the transmitter technology: as an example, Fig. 1.4 shows a Mars downlink budget laser trade, as reported in [6]. Each of the available laser transmitters have advantages for some aspects, and disadvantages for others. Between them, one of the most important aspect is that, given a detection system, certain wavelengths can give higher detection efficiency than anothers. Some wavelengths have also been preferred because of the availability of good transmitter and detector systems.

It is also important to notice some preferred wavelengths: solid-state laser and fiber-amplified laser have functionality in a range of wavelengths between 1000 nm to 2000 nm. The 1064 nm and 1550 nm lasers have been commonly used in many space missions, for their characteristic to be very efficient in respect to the detectors technologies. For example, ESA's EDRS transmitter laser is a Nd:YAG type, used with a frequency of 1064 nm [7]. However, as described in table II [8], other wavelength values have been used for optical

inter-satellite and deep-space communications, such as 1058 nm and 1076 nm; values lower than 1000 nm have been also used, such as 532 nm, and 830 nm using a laser diode.

1.2.2 Spacecraft Telescope

A common optical antenna geometry, employed to send and collect optical signals in space, is shown in Fig.1.5, where the laser is a TEM00 single spatial-mode beam [9]. The telescope consists of two mirrors, named primary and secondary, with radius a and b respectively. The laser pulse transmitted bounces off the secondary mirror, is scattered on the primary mirror, and then is reflected in open-space. This operation is equal to the one of a classic parabola, with the difference that for optical frequency signals it is necessary to use mirrors. Optical antennas are also much smaller than the RF ones, because of the previous considerations about the wavelength and the narrow primary lobe for the focusing. For those reasons, the whole optical transmission system has a smaller cost and weight respect the RF systems.

In Fig. 1.5, the $1/e^2$ Gaussian width is denoted with w, and it represents the distance between the two points of the Gaussian laser profile that are the $1/e^2 = 0.135$ times the maximum value. This type of shape overfills the antenna aperture, so the parameter $\alpha = a/w$ represents the losses respect the primary profile.
The presence of the secondary mirror has the side-effect to block part of the radiation incident on the primary mirror. Parameter $\gamma = b/a$ describes this obscuration loss.

From the definition of antenna gain as the ratio between the intensity radiated in the axis direction, $I(r, \theta)$, and the isotropic radiation, I_0, the

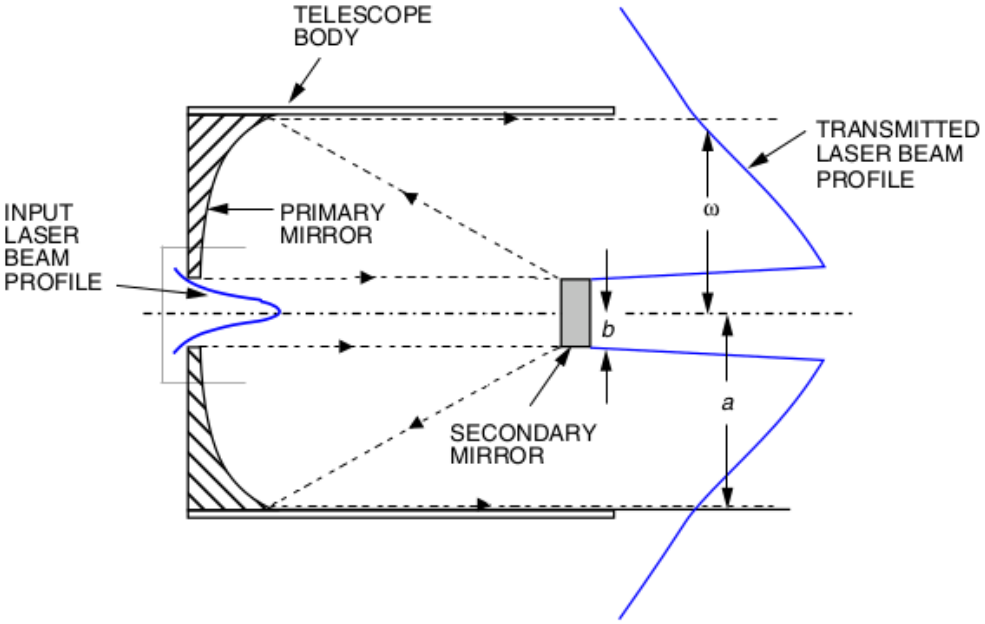

Figure 1.5: Optical antenna geometry [9]

transmitter gain can be derived as

$$\begin{aligned} G_{\text{tx}} &= \frac{I(r,\theta)}{I_0} \\ &= \frac{4\pi A}{\lambda^2}\,\eta_{\text{tx}} \end{aligned} \tag{1.5}$$

where r and θ define the observation point, A is the area of the primary mirror and λ the laser wavelength. The efficiency $\eta_{\text{tx}} = \eta_{\text{tx}}(\alpha, \beta, \gamma, X)$ depends on the obscuration loss and on the overfill losses, while β and X have dependencies on the observing point and the radius of curvature of the beam.
If the antenna is considered in reception, it is possible to define the receiving gain as

$$G_{\text{rx}} = \frac{4\pi A}{\lambda^2}\left(1-\gamma^2\right) \tag{1.6}$$

where it is explicitly shown the obscuration loss [9, 10].

1.2.3 Acquisition, Tracking and Pointing

As previously described, the pointing between the two antennas has to be very accurate because of the narrow radiation primary lobe of the transmitting antenna system. For this reason, pointing losses are very critical in optical communication links, where small errors (i.e., of the μrad order) in the angular precision can lead to very important gain drops.

For the analysis of tracking errors for deep-space, the point-ahead must considered. This is the angle orientation of the receiving system at the laser transmission time, which is not trivial to predict, due the great distance between the two units. Nowadays, the calculation of the point-ahead is very accurate, and it can be achieved using the Ephemerides data [11].
Moreover, it must be taken into account the dominant source of spatial tracking errors, which is the mechanical noise due to vibrations and motions of the satellite.

Therefore, in order to align the two antennas and achieve the mutual line of sight (LOS), it is possible to use a beacon signal and a closed-loop spatial tracking system. The beacon signal can be implemented directly in the data transmission, or be another different beam laser. A possible scheme for the tracking system is shown in Fig. 1.6 [11]. Note that the delay due to the long distances should be taken into account.
In section 1.4 the pointing losses will be explained in detail.

1.2.4 Detectors

Detector systems play a key role in the optical link technological implementation. Their function is to measure photons arriving at the receiving satellite and to generate a signal that can be processed by the demodulation and decoding system.
There are mainly two detection schemes, named coherent and direct detection, that differ for some aspects. While the former is more resistant from background noise and, theoretically, has good performance on the link

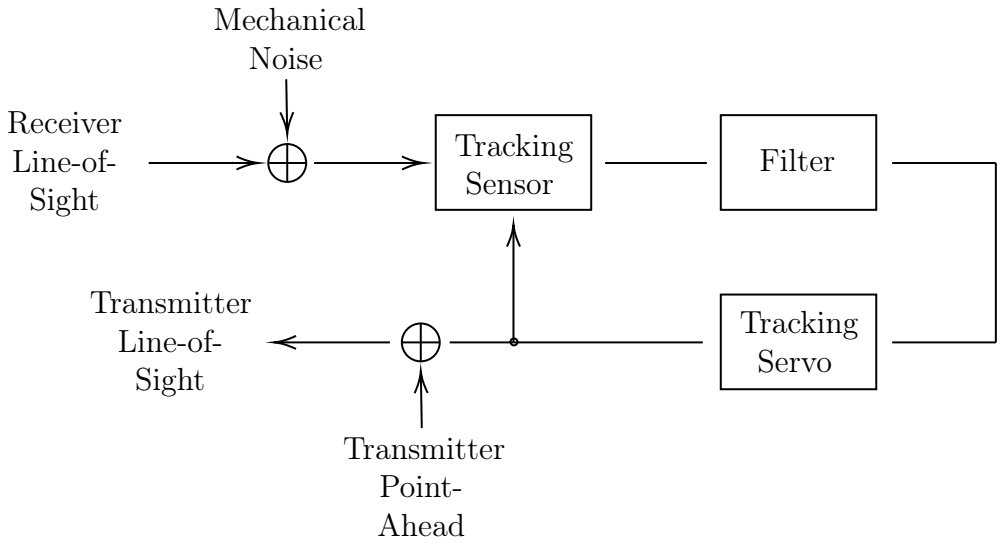

Figure 1.6: Closed-loop spatial tracking system.

budget, the latter is more simple [7, 12]. The detection technique and the potential use of pre-amplifiers also determine the background noise level at the receiver (besides the other noise sources): shot noise is the dominant source of noise for the coherent detection scheme, due to the local oscillator; instead, for direct scheme there is no a prevailing noise, being affected by detector dark currents, amplifier noise, and thermal noise [8]. Direct detection schemes will be assumed here for deep-space implementations [9].

Besides the detection scheme choice, it is also necessary to select the device that allows photons detection and their conversion into an electrical signal. Avalanche photodiode detectors (APDs), positive-intrinsic-negative (PIN) photodiodes, and photomultiplier tubes (PMTs) are examples of detectors used in optical PPM receiver design. APD exhibits a bigger sensitivity than PIN photodiodes, but also presents a smaller gain, therefore it is hardly employed in high thermal noise systems; PMT instead, in addition to the direct detection, seems to be suited for deep space environments thanks to the higher gain, making possible the detection of individual photons [13].
In Fig. 1.7 is shown a common use of the PMT device, which detects and integrates a certain number of photons over a time slot. Every time a photon

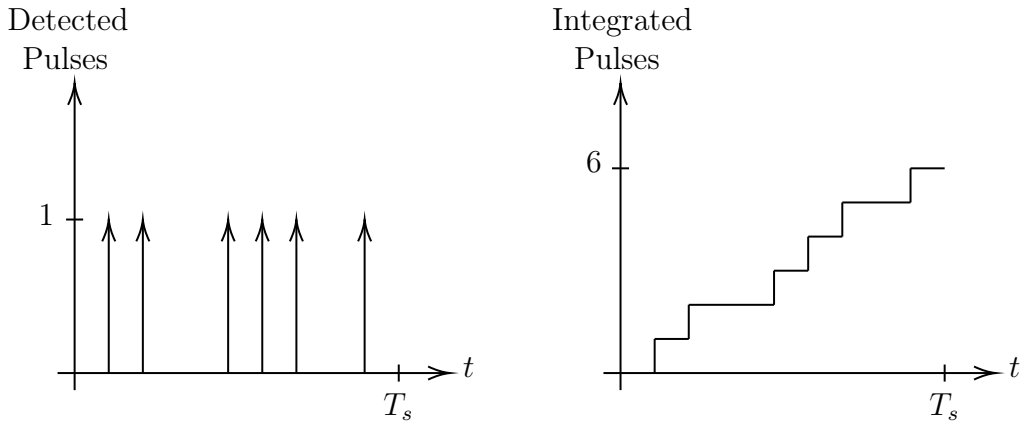

Figure 1.7: Pulse stream integration of a PMT device.

collides the surface of the device, this outputs an electrical pulse. In order to determine if a photon has collided or not, a threshold is set. This has to be fixed in a precise way: not too high, because no photons will be detected, and not too low, because the device must differentiate the arrival of photons from the thermal noise.

1.3 Power Losses

In the realization and implementation of an optical communication link between two satellites, various losses have to be considered. The final goal is the choice of technologies, signal coding and modulation parameters able to achieve a working and stable exchange of information.
In a deep-space optical communication link, two losses are critical: pointing and space losses. The first kind of losses will be better explained in section 1.4.

It can be possible describe the space losses starting from the Friis formula for free-space gain

$$L_{\text{space}} = \left(\frac{\lambda}{4\pi d}\right)^2 \tag{1.7}$$

where d is the distance between the transmitting and receiving antennas. Although equation (1.7) is a gain (received power to transmitted power), we will after refer to it as a loss. Space losses are inversely proportional to the square of distance, therefore in deep-space attenuation is a key variable in the power budget. For deep-space links it is common to explicit distances in astronomical unit (AU); an AU corresponds to 149597871 Km, that is approximately the distance between Earth and the Sun (originally defined as a mean value of the variable distance between them, this definition has been determined since 2012).

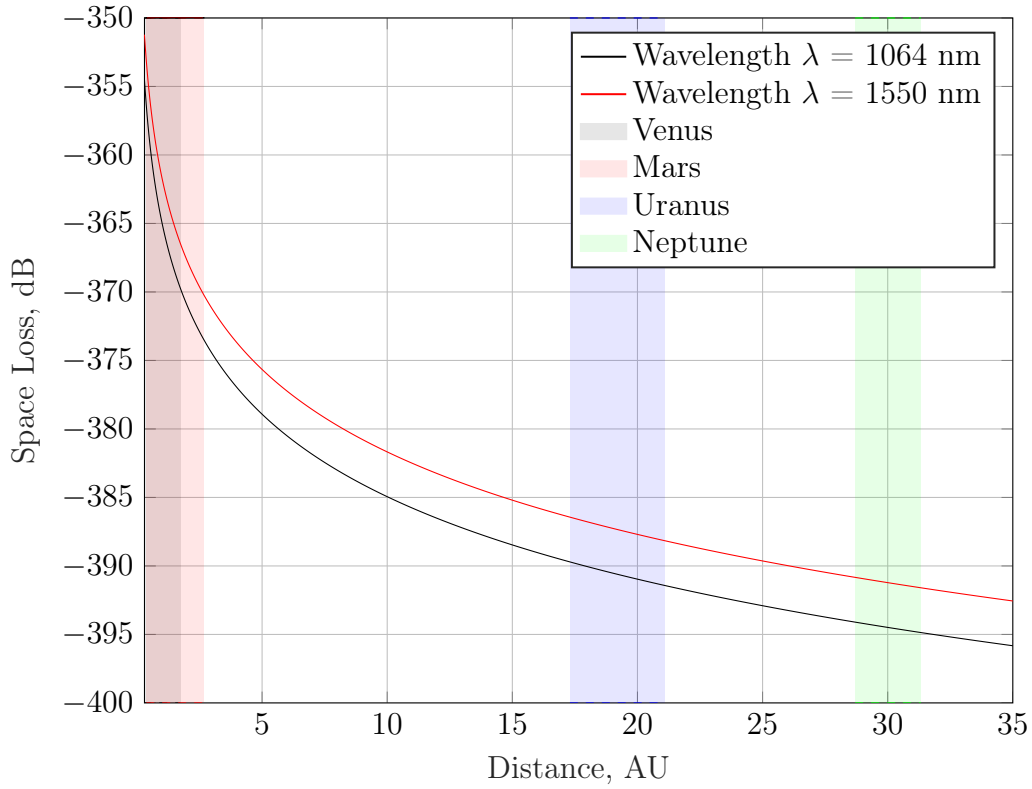

Figure 1.8: Free-space loss, dependence on distance.

In Fig. 1.8 it is possible see the evolution of equation (1.7) for different values of distance. The semi-transparent areas indicate the distance ranges from Earth of the four planets (Venus, Mars, Uranus, and Neptune). For example, Neptune is about 31.33 AU far away from Earth in its farther position, and about 28.7 AU in its nearest position. The link budgets in chapter 3 will

report the worst case distances.
The graph gives an idea of the space losses given a distance and a wavelength: as an example, using a laser wavelength of 1064 nm, a loss of $L_{\text{space}} = 395$ dB must be considered for Neptune worst case.
Fig. 1.8 also shows the dependence of space losses on the laser wavelength. As equation (1.7) shows, there is a direct proportionality between L_{space} and the square of λ, that means a lower frequency will generate less space losses than an higher one. Therefore, there is another trade off between a bigger antenna gain and an extra losses in the power budget: choosing a bigger wavelength, then using a smaller laser frequency, results in a smaller space losses, but also in a smaller antenna gain.

Transmitting and receiving system efficiencies must also be considered [9]. Laser transmission losses are caused by the coupling of the signal with the optical system and its propagation through the telescope. In receiving phase, it is necessary to include primary- and secondary-mirror losses, truncation losses due to the overfilling of the beam into the receiving aperture, narrow bandpass filter losses and polarization offset. Usually, all of these non-ideality effects are considered in a unique parameter named efficiency, whose value is included between 0 and 1, and it is multiplied to the antenna gain. The transmitting and receiving efficiencies are denoted respectively as η_{tx} and η_{rx}.

Another type of losses are those related to the detection system and to other implementation non-ideality.
Detection losses can be connected to the device threshold, therefore to the miss-detection of transmitted photons. They can also be related to the laser coupling with the decoder.
Implementation losses, instead, represent the differences between a simulation done in a local computer or server, and the implementation of the system in a real environment. For example, as will be better explained in chapter 2 and 4, two C++ simulators have been written in order to simulate the entire coding and modulating system, with the use of 64 bit fixed point variables; here, there are no memory or time problems, so it can be possible using large

bit precision or launch the simulation for a large number of decoding iterations (that is a parameter explained in the respective chapters). Instead, in a real satellite environment it can be possible that the memory allocation is restricted, so the bit precision can influence the performance of the system. Moreover, the time to process the received signals is limited; even energy spent for a frame decoding must be considered. For these reasons, some dB of loss must be taken into account.

1.4 Pointing Losses

From the assumptions of section 1.2.3, it is possible to estimate independently the two angular errors (azimuth and elevation) by using a quadrant detector. In this way, these two angles can be modelled as zero mean independent Gaussian random variables [11]. Therefore, the resulting random radial tracking error $\mathsf{\theta}$, which is the angle between the LOS and the pointing direction, is distributed according to a Rayleigh distribution

$$f_{\mathsf{\theta}}(\theta) = \frac{\theta}{\sigma_\theta^2}\, e^{-\theta^2/2\sigma_\theta^2} \tag{1.8}$$

where σ_θ^2 is the parameter describing the angular noise. In particular, using the system in Fig. 1.6 it is possible to obtain

$$\sigma_\theta^2 = \frac{1}{2\pi}\int_{-\infty}^{\infty} S_\theta(\omega)\,|1 - H_{\mathrm{T}}(\omega)|^2\, d\omega \tag{1.9}$$

where $S_\theta(\omega)$ is the power spectral density of the residual mechanical noise and $H_{\mathrm{T}}(\omega)$ is the transfer function of the tracking system [11].

For the link power budget, the tracking error is the only random quantity. Then, we can define a outage probability P_{out}, which is the probability that the losses due to the pointing, L_{p}, exceed the link margin $\mathcal{M}$

$$P_{\mathrm{out}} = \mathbb{P}\{-L_{\mathrm{p}}[dB] > \mathcal{M}[dB]\}\ . \tag{1.10}$$

In the optical scenario the link margin is given by $\mathcal{M} = n_s[dB] - n_{s,min}[dB]$, where n_s is the average received number of signal photons per second and $n_{s,min}$ is the minimum average number of signal photons per second which allows a certain target error probability of the communication system. There are several models taking into account the pointing error. These errors can be interpreted as a gain loss due to the miss-alignment with the antenna boresight. In Fig. 1.9 are reported the models we are considering used in the case of parabolic antenna.

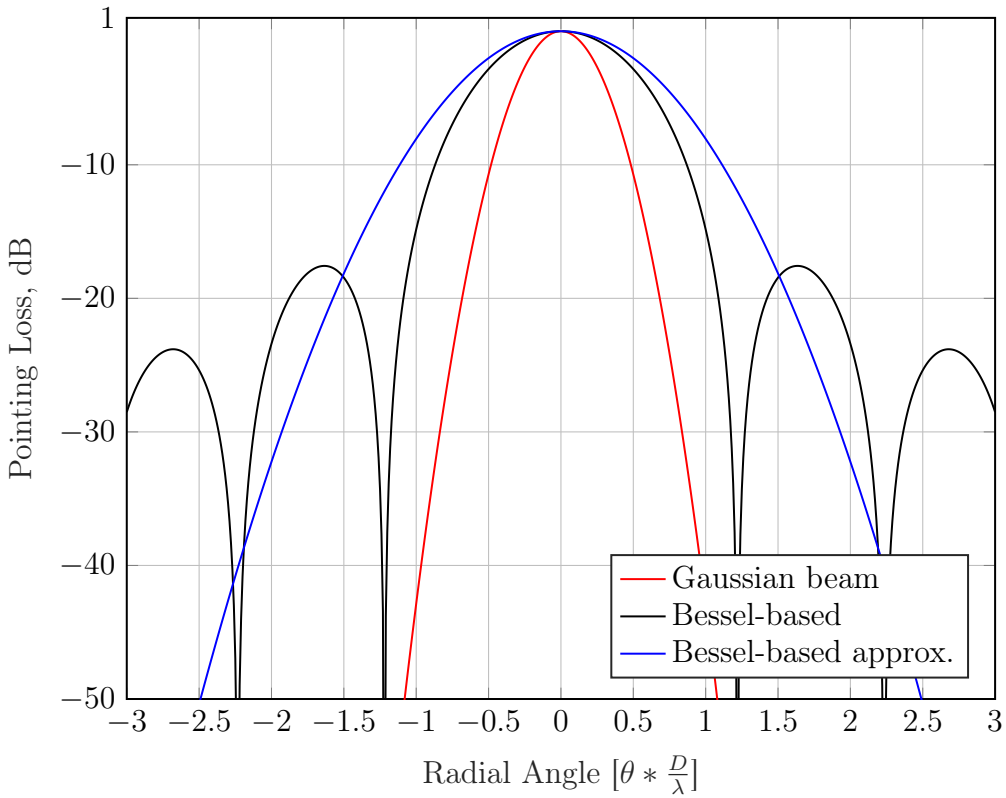

Figure 1.9: Comparison between different pointing loss models.

Since the two satellites are both in movement, it is necessary to consider the pointing problem for each of them. Due to these considerations, in the following sections different models are considered in the case where both the systems introduce pointing errors.

1.4.1 Gaussian Beam Model

The model used in the case of Gaussian beam to describe the pointing losses of an antenna with linear gain G is given by [11]

$$L_{\mathrm{p}}(\theta) = e^{-G\theta^2} \,. \tag{1.11}$$

Hence, considering the same system tracking accuracy defined by σ_θ for both the transmitter and the receiver, it is possible to write

$$\begin{aligned} P_{\mathrm{out}} &= \mathbb{P}\Big\{-10\log_{10}\Big(L_{\mathrm{p,t}}(\theta_{\mathrm{t}})\Big) - 10\log_{10}\Big(L_{\mathrm{p,r}}(\theta_{\mathrm{r}})\Big) > \mathcal{M}\Big\} \\ &= \mathbb{P}\big\{G_{\mathrm{t}}\theta_{\mathrm{t}}^2 + G_{\mathrm{r}}\theta_{\mathrm{r}}^2 > K\big\} \end{aligned} \tag{1.12}$$

where $K = \frac{ln(10)}{10}\,\mathcal{M}[dB]$ and the subscripts t and r indicates respectively the transmitter and the receiver. The random variables θ_{t} and θ_{r} are independent and identically distributed according to (1.8). Then $\mathsf{y}_{\mathrm{r}} = \theta_{\mathrm{r}}^2$ and $\mathsf{y}_{\mathrm{t}} = \theta_{\mathrm{t}}^2$ are independent and identically distributed according to an exponential distribution with mean $2\sigma_\theta^2$. Therefore

$$\begin{aligned} P_{\mathrm{out}} &= 1 - \int_0^{K/G_{\mathrm{r}}} \int_0^{\frac{K-G_{\mathrm{r}}y_{\mathrm{r}}}{G_{\mathrm{t}}}} \frac{1}{2\sigma_\theta^2}\, e^{-\frac{y_{\mathrm{t}}}{2\sigma_\theta^2}} \frac{1}{2\sigma_\theta^2}\, e^{-\frac{y_{\mathrm{r}}}{2\sigma_\theta^2}}\, dy_{\mathrm{t}} dy_{\mathrm{r}} \\ &= 1 - \int_0^{K/G_{\mathrm{r}}} \Big(1 - e^{-\frac{K-G_{\mathrm{r}}y_{\mathrm{r}}}{2\sigma_\theta^2 G_{\mathrm{t}}}}\Big) \frac{1}{2\sigma_\theta^2}\, e^{-\frac{y_{\mathrm{r}}}{2\sigma_\theta^2}}\, dy_{\mathrm{t}} dy_{\mathrm{r}} \\ &= e^{-K/2\sigma_\theta^2 G_{\mathrm{r}}} + e^{-K/2\sigma_\theta^2 G_{\mathrm{t}}} \int_0^{K/G_{\mathrm{r}}} \frac{1}{2\sigma_\theta^2}\, e^{-y_{\mathrm{r}}\frac{G_{\mathrm{t}}-G_{\mathrm{r}}}{2\sigma_\theta^2 G_{\mathrm{t}}}}\, dy_{\mathrm{r}} \\ &= \frac{G_{\mathrm{t}}}{G_{\mathrm{t}} - G_{\mathrm{r}}}\, e^{-K/2\sigma_\theta^2 G_{\mathrm{t}}} - \frac{G_{\mathrm{r}}}{G_{\mathrm{t}} - G_{\mathrm{r}}}\, e^{-K/2\sigma_\theta^2 G_{\mathrm{r}}} \,. \end{aligned} \tag{1.13}$$

In particular, if $G = G_{\mathrm{t}} = G_{\mathrm{r}}$, the equation (1.13) can be written as

$$P_{\mathrm{out}} = \left(1 + \frac{K}{2\sigma_\theta^2 G}\right) e^{-K/2\sigma_\theta^2 G} \,. \tag{1.14}$$

From equation (1.14) it is possible to derive, using numerical methods, the $\sigma_{\theta,\max}$ which guarantees the specified P_{out} given the antennas gain G and the link margin $\mathcal{M}$.

It is important to note that, from (1.13) it is possible to study also the particular case where a single antenna introduces a miss-pointing error with the hypothesis that $G_{\mathrm{R}} \to 0$ (or $G_{\mathrm{T}} \to 0$). The same result can be obtained without this assumption, starting from $P_{\mathrm{out}} = \mathbb{P}\{G\theta^2 > K\}$, giving

$$P_{\mathrm{out}} = e^{-K/2\sigma_\theta^2 G}\,. \tag{1.15}$$

This scenario can be used when a loss dominates the other or simply when the pointing error in one side is negligible.

Tab. 1.1 and 1.2 show some values of $\sigma_{\theta,\max}$, which is the σ_θ that guarantees the specified P_{out}, respectively for a fixed antenna gain and a fixed link margin. In Tab. 1.1, gains are imposed to 120 dB for both the antennas; choosing a link margin value and a target outage probability, with the bisection method and using the equation (1.14) it is possible to find the maximum σ_θ for which the system will be on outage for the specified amount of time. For example, if a 4 dB link margin and a 5% probability of outage are requested, the $\sigma_{\theta,\max}$ will be 0.312 μrad.
Tab. 1.2 has conceptually the same meaning of the previous one, with the difference that a 4 dB link margin is fixed and $\sigma_{\theta,\max}$ is variable for different values of antenna gains. For example, if both transmitting and receiving antennas have a 130 dB gain, $\sigma_{\theta,\max}$ will be equal to 0.099 μrad for a 5% outage probability.
As expected, the pointing will be more tight as the outage probability will be reduced; on the other hand, pointing requirements will be loosen as the link margin becomes bigger. As cited in previous paragraph, antennas with a large diameter will have more gain, with the primal lobe very directive, so the pointing requirements will be very tighten.

P_{outage} / LM[dB]	25%	10%	5%	1%
2.00	0.292	0.243	0.220	0.186
3.00	0.358	0.298	0.270	0.228
4.00	0.414	0.344	0.312	0.263
5.00	0.462	0.385	0.348	0.294
6.00	0.507	0.421	0.382	0.323
7.00	0.547	0.455	0.412	0.348
8.00	0.585	0.487	0.441	0.372
9.00	0.620	0.516	0.467	0.395
10.00	0.654	0.544	0.493	0.416

Table 1.1: $\sigma_{\theta,\max}$, in μrad, requested to satisfy a given outage probability and a given link margin. Fixed antennas gain at 120 dB. Gaussian beam model.

P_{outage} / Gain[dB]	25%	10%	5%	1%
110.00	1.308	1.088	0.985	0.833
115.00	0.735	0.612	0.554	0.468
120.00	0.414	0.344	0.312	0.263
125.00	0.233	0.193	0.175	0.148
130.00	0.131	0.109	0.099	0.083
135.00	0.074	0.061	0.055	0.047
140.00	0.041	0.034	0.031	0.026

Table 1.2: $\sigma_{\theta,\max}$, in μrad, requested to satisfy a given outage probability and a given antennas gain. Fixed link margin at 4 dB. Gaussian beam model.

1.4.2 Circular Aperture Approximation Model

The following model is an approximation of the model described in the next section [14]. We firstly introduce this approximation because it is used in the numerical method developed to compute the outage probability of the circular aperture model. In fact, for small θ, we can write

$$\left(\frac{2\,J_1(\sqrt{G}\theta)}{\sqrt{G}\theta}\right)^2 \simeq e^{-\alpha G\theta^2}\,. \tag{1.16}$$

where $\alpha = 0.188$. Hence, considering the same system tracking accuracy defined by σ_θ for both the transmitter and the receiver, the procedure to compute the outage probability is the same adopted in section 1.4.1

$$P_{\text{out}} = \mathbb{P}\left\{\alpha G_{\text{t}}\theta_{\text{t}}^2 + \alpha G_{\text{r}}\theta_{\text{r}}^2 > K\right\} \tag{1.17}$$

where $K = \frac{ln(10)}{10}\,\mathcal{M}[dB]$ and the subscripts t and r indicates respectively the transmitter and the receiver. Again, considering $\mathsf{\theta}_{\text{t}}$ and $\mathsf{\theta}_{\text{r}}$ independent and identically distributed according to (1.8), the random variables $\mathsf{y}_{\text{r}} = \mathsf{\theta}_{\text{r}}^2$ and $\mathsf{y}_{\text{t}} = \mathsf{\theta}_{\text{t}}^2$ are independent and identically distributed according to an exponential distribution with mean $2\sigma_\theta^2$. Therefore

$$P_{\text{out}} = \frac{G_{\text{t}}}{G_{\text{t}} - G_{\text{r}}}\,e^{-K/2\sigma_\theta^2\alpha G_{\text{t}}} - \frac{G_{\text{r}}}{G_{\text{t}} - G_{\text{r}}}\,e^{-K/2\sigma_\theta^2\alpha G_{\text{r}}}\,. \tag{1.18}$$

In particular, if $G = G_{\text{t}} = G_{\text{r}}$, the equation (1.18) can be written as

$$P_{\text{out}} = \left(1 + \frac{K}{2\sigma_\theta^2\alpha G}\right)\,e^{-K/2\sigma_\theta^2\alpha G}\,. \tag{1.19}$$

Tab. 1.3 and Tab. 1.4 show some values of $\sigma_{\theta,\max}$ respectively for a fixed antenna gain and a fixed link margin. In Tab. 1.3, gains are imposed to 120 dB for both the antennas; choosing a link margin value and an outage probability requirement, with the bisection method and using equation (1.19) it is possible to find the maximum σ_θ for which the system will be on outage for the specified amount of time. Tab. 1.4 has a 4 dB link margin fixed

and $\sigma_{\theta,\max}$ is variable for different values of antenna gains. As expected, the pointing requirements for the circular aperture approximation model is more favorable than the one described in the previous sub-paragraph. For example, chosen a 4 dB link margin and an outage probability of 5% for both the method, a $\sigma_{\theta,\max}$ equal to 0.719 μrad and 0.312 μrad results, respectively for the circular aperture approximation and for the Gaussian beam models.

P_{outage} / **LM[dB]**	25%	10%	5%	1%
2.00	0.674	0.561	0.508	0.429
3.00	0.826	0.687	0.622	0.526
4.00	0.954	0.794	0.719	0.607
5.00	1.066	0.887	0.803	0.679
6.00	1.168	0.972	0.880	0.744
7.00	1.262	1.050	0.951	0.804
8.00	1.349	1.122	1.016	0.859
9.00	1.431	1.190	1.078	0.911
10.00	1.508	1.255	1.136	0.960

Table 1.3: $\sigma_{\theta,\max}$, in μrad, requested to satisfy a given outage probability and a given link margin. Fixed antennas gain at 120 dB. Circular aperture model approximation

P_{outage} / **Gain[dB]**	25%	10%	5%	1%
110.00	3.016	2.509	2.272	1.921
115.00	1.696	1.411	1.278	1.080
120.00	0.954	0.794	0.719	0.607
125.00	0.536	0.446	0.404	0.342
130.00	0.302	0.251	0.227	0.192
135.00	0.170	0.141	0.128	0.108
140.00	0.095	0.079	0.072	0.061

Table 1.4: $\sigma_{\theta,\max}$, in μrad, requested to satisfy a given outage probability and a given antennas gain. Fixed link margin at 4 dB. Circular aperture model approximation

1.4.3 Circular Aperture Model

Another useful model describing the pointing losses is given by

$$L_{\mathrm{p}}(\theta) = \left(\frac{2\, J_1(\sqrt{G}\theta)}{\sqrt{G}\theta} \right)^2 \tag{1.20}$$

used in [11, 15]. Hence, considering the same system tracking accuracy defined by σ_θ for both the transmitter and the receiver, it is possible to write

$$P_{\mathrm{out}} = \mathbb{P}\Big\{ -10\log_{10}\Big(L_{\mathrm{p,t}}(\theta_{\mathrm{t}})\Big) - 10\log_{10}\Big(L_{\mathrm{p,r}}(\theta_{\mathrm{r}})\Big) > \mathcal{M} \Big\}\,. \tag{1.21}$$

Differently from section 1.4.1, it is not possible to derive P_{out} in closed form. Then, in Algorithm 1, a numerical method is described to compute P_{out}. Usually the outage probability is a given parameter and the goal is to compute

Algorithm 1: Numerically derive P_{out} due to pointing losses

Result: P_{out} for the circular aperture model;

Input: σ_θ parameter, transmitter gain G_{t}, receiver gain G_{r}, link margin $\mathcal{M}$;

1) Construct a pmf which approximate the Rayleigh distribution of the angle θ;
2) Map this angular pmf into the transmitter and receiver losses pmf according to $L_{\mathrm{p,t}}(\theta_{\mathrm{t}})$ and $L_{\mathrm{p,r}}(\theta_{\mathrm{r}})$;
3) Exploiting the independence of random variables, construct the joint pmf of the pointing losses;
4) Sum the probability which satisfy the event

$$\mathcal{E} = \Big\{ -10\log_{10}\Big(L_{\mathrm{p,t}}(\theta_{\mathrm{t}})\Big) - 10\log_{10}\Big(L_{\mathrm{p,r}}(\theta_{\mathrm{r}})\Big) \leqslant \mathcal{M} \Big\} \tag{1.22}$$

and finally, $P_{\mathrm{out}} = 1 - \mathbb{P}\{\mathcal{E}\}$;

$\sigma_{\theta,\max}$ which guarantees the specified P_{out}. Hence, the numerical procedure in Algorithm 2 has been implemented.

Algorithm 2: Numerically derive $\sigma_{\theta,\max}$ of the pointing system

Result: $\sigma_{\theta,\max}$ for the circular aperture model;

Input: outage probability target $P_{\text{out}}^{(\text{T})}$, transmitter gain G_{t}, receiver gain G_{r}, link margin $\mathcal{M}$;

1) Compute σ_1 from the Gaussiam beam model (lower bound);
2) Compute σ_2 from the circular aperture approximation model (upper bound);
3) Define the function $g(\sigma_\theta) = P_{\text{out}}(\sigma_\theta) - P_{\text{out}}^{(\text{T})}$, where $P_{\text{out}}(\sigma_\theta)$ is computed using Algorithm 1;
4) Perform the bisection procedure of the function $g(\sigma_\theta)$ in the interval $[\sigma_1, \sigma_2]$ to obtain $\sigma_{\theta,\max}$;

Tab. 1.5 and Tab. 1.6 show the $\sigma_{\theta,\max}$ respectively for a fixed antenna gain and fixed link margin. In Tab. 1.5, gains are imposed to 120dB for both the antennas; choosing a link margin value and an outage probability requirement it is possible to find the maximum σ_θ for which the system will be on outage for the specified amount of time. Tab. 1.6 has a 4 dB link margin fixed and $\sigma_{\theta,\max}$ is variable for different values of antenna gains. As expected, pointing requirements for the circular aperture method are intermediate compared with the other, in relation to Fig. 1.9.

P_{outage} / LM[dB]	25%	10%	5%	1%
2.00	0.577	0.480	0.435	0.367
3.00	0.702	0.584	0.529	0.447
4.00	0.805	0.670	0.607	0.513
5.00	0.894	0.744	0.673	0.569
6.00	0.973	0.809	0.733	0.619
7.00	1.043	0.868	0.785	0.664
8.00	1.107	0.921	0.834	0.704
9.00	1.165	0.969	0.878	0.742
10.00	1.219	1.014	0.918	0.776

Table 1.5: $\sigma_{\theta,\max}$, in μrad, requested to satisfy a given outage probability and a given link margin. Fixed antenna gain at 120 dB. Circular aperture model

P_{outage} / Gain[dB]	25%	10%	5%	1%
110.00	2.546	2.118	1.918	1.621
115.00	1.432	1.191	1.079	0.912
120.00	0.805	0.670	0.607	0.513
125.00	0.453	0.377	0.341	0.288
130.00	0.255	0.212	0.192	0.162
135.00	0.143	0.119	0.108	0.091
140.00	0.080	0.067	0.061	0.051

Table 1.6: $\sigma_{\theta,\max}$, in μrad, requested to satisfy a given outage probability and a given antenna gain. Fixed link margin at 4 dB. Circular aperture model

Chapter 2

Coded Modulation for Optical Links

The SCPPM scheme refers to a precise combination of modulation and coding technique mostly used in a deep-space optical link scenario, because of its characteristics that suit well for this environment, as explained in section 1.1. The name SCPPM derives from the combination of a PPM modulator along with other blocks serially concatenated to it. Between them, an error-control code have been chosen between different solutions: Reed-Solomon codes and convolutional codes have been tested [2]. In particular, a variant of the convolutional coded PPM have been demonstrated to reach good performances: the introduction of an accumulator and of an interleaver blocks, with the implementation of an iterative decoding algoritmh, differs from other basic tested approaches.

2.1 Encoder

Fig. 2.1 shows the block diagram of the SCPPM encoder system. User data firstly enters in a cyclic redundancy check (CRC) block, that appends 32 binary digits at the end of each prefixed length bit stream $\mathbf{d}$. Calling j the index that goes from 0 to $k + 31$, where k is the length of $\mathbf{d} = \{d_0, d_1, \ldots, d_{k-1}\}$,

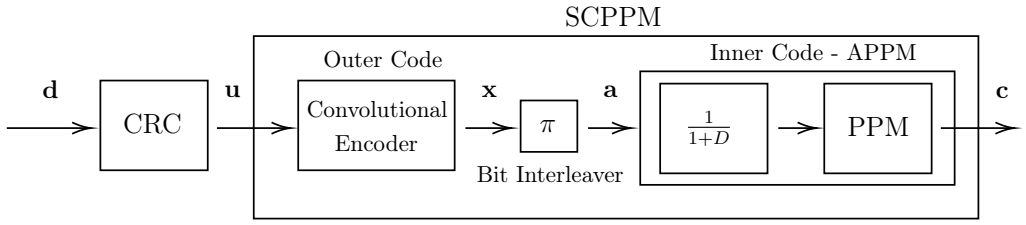

Figure 2.1: Conceptual scheme of the SCPPM encoder [2].

the vector $\mathbf{u} = \{u_0, u_1, \ldots, u_{k-1}, \ldots, u_{k+31}\}$ can be written as

$$u_j = \begin{cases} d_j, & \text{if } 0 \leqslant j < k \\ z_j, & \text{if } k \leqslant j < k + 32. \end{cases} \tag{2.1}$$

The value of the length k will be explained next. The CRC attachment, $\mathbf{z}$, is given by

$$\mathbf{z}(X) = \mathbf{d}(X) \bmod \mathbf{h}(X) \tag{2.2}$$

where $\mathbf{z}(X)$ and $\mathbf{d}(X)$ are the polynomial notation of the CRC attachment and of the user data bit vector, respectively

$$\begin{aligned} \mathbf{z}(X) &= z_0 X^{31} + z_1 X^{30} + \cdots + z_{30} X + z_{31} \\ \mathbf{d}(X) &= d_0 X^{k+31} + d_1 X^{k+30} + \cdots + d_{k-2} X^{33} + d_{k-1} X^{32}. \end{aligned} \tag{2.3}$$

In equation (2.2) all the arithmetic is module two, and $\mathbf{h}(X)$ is the generator polynomial given by

$$\mathbf{h}(X) = X^{32} + X^{29} + X^{18} + X^{14} + X^3 + 1. \tag{2.4}$$

The CRC attachment will be used in the receiving phase for the evaluation of the correct decoding of the codeword.

After that, vector $\mathbf{u}$ is convolutionally coded. The consultative committee for space data systems (CCSDS) recommendation for space data system standards cite that this encoder, also denoted as outer code, shall be

a constraint-length-three convolutional code, and its generator polynomials are $\mathbf{g} = [5, 7, 7]$ in octal notation, or

$$\begin{aligned} \mathrm{g}^{(1)}(D) &= 1 + D^2 \\ \mathrm{g}^{(2)}(D) &= 1 + D + D^2 \\ \mathrm{g}^{(3)}(D) &= 1 + D + D^2 \end{aligned} \tag{2.5}$$

generating a 1/3 code rate. This basic encoder can be punctured in order to achieve also rate 1/2 or 2/3; the puncture patterns is described in Tab. 2.1. The resulting codeword must have a fixed length of $\widehat{k} = 15120$ bits. This

Rate	P_0	P_1	P_2	P_3	P_4	P_5
1/3	1	1	1	1	1	1
1/2	1	1	0	1	1	0
2/3	1	1	0	0	1	0

Table 2.1: Convolutional encoder puncture patterns

value shall be predetermined in order to allow flexibility in the choice of the code rates, and to implement a single interleaver. So, vector **u** length must change in relation to the convolutional code rate, and at the same time must consider the CRC bit attachment and the termination bits. The latter are needed for the re-initialization of the encoder state, for which every vector **u** starts with the "all-zeroes" state. It can be proved that for each code rate the termination bits are two. So, vector **u** length, k^*, must be k+32+2, as described in Tab. 2.2.

Rate	k	k^*	$\widehat{k}$
1/3	5006	5040	15120
1/2	7526	7560	15120
2/3	10046	10080	15120

Table 2.2: Relationship between **u** length and convolutional code rates.

After the codeword $\mathbf{x} = \{x_0, x_1, \ldots, x_{\widehat{k}-1}\}$ has been generated, it must be

interleaved. The permutation produces a vector $\mathbf{a}$, where a_j is the j^{th} binary symbol permuted, and it is equal to the $\pi(j)^{th}$ symbol of the codeword $\mathbf{x}$, where

$$\pi(j) = \left(11j + 210j^2\right) \bmod 15120 \tag{2.6}$$

is a possible second-degree permutation polynomial choice.

The permuted bits are successively elaborated by the accumulator PPM (APPM) block, also named inner code, composed by an accumulator and a memoryless PPM modulator. The accumulator can also be described as a rate-one code with transfer function $1/(1+D)$. Fig. 2.2 shows the block scheme of the accumulator, that takes as input each binary symbol of codeword $\mathbf{a} = \{a_0, a_1, \ldots, a_{\widehat{k}-1}\}$ and generates the vector $\mathbf{b} = \{b_0, b_1, \ldots, b_{\widehat{k}-1}\}$, with the rule described as

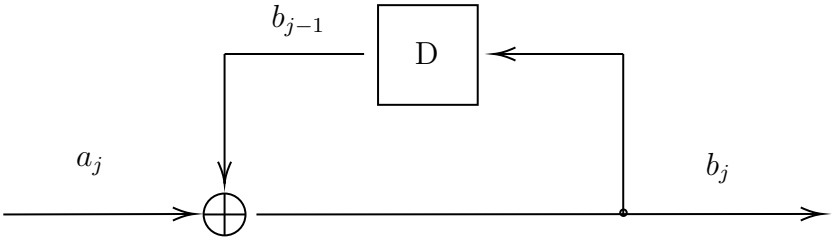

Figure 2.2: Accumulator block scheme.

$$b_j = \begin{cases} a_j, & \text{if } j = 0 \\ a_j \oplus b_{j-1}, & \text{if } 1 \leqslant j < 15120 \end{cases} \tag{2.7}$$

where the symbol $\oplus$ identifies the module two sum between the two bits. The accumulator shall be initialized at the zero-state for each input codeword, as the first condition of equation (2.7) suggests.

Finally, vector $\mathbf{b}$ passes through the pulse-position modulator. The codeword is fractioned in $S = 15120/m$ symbols, where $m = \log_2 M$, with M the PPM orded. The CCSDS recommendation defines the possible value of M

			PPM pulse position		
State	**a**	**b**	Natural	Gray	Anti-Gray
0	000	000	0	0	0
0	001	111	7	7	5
0	010	110	6	3	6
0	011	001	1	4	3
0	100	100	4	1	2
0	101	011	3	6	7
0	110	010	2	2	4
0	111	101	5	5	1
1	000	111	7	7	5
1	001	000	0	0	0
1	010	001	1	4	3
1	011	110	6	3	6
1	100	011	3	6	7
1	101	100	4	1	2
1	110	101	5	5	1
1	111	010	2	2	4

Table 2.3: Different type of PPM mapping [2].

as $M = \{4, 8, 16, 32, 64, 128, 256\}$. The output of the PPM block is a slotted symbol sequence $\mathbf{c} = \{c_0^{q_0}, c_1^{q_1}, \ldots, c_{S-1}^{q_{S-1}}\}$, where each $\mathbf{c}_i^{q_i}$ represent a PPM symbol with a laser pulse in the q_i position. Vector $\mathbf{q} = \{q_0, q_1, \ldots, q_{S-1}\}$ defines the integer position values, in the range between 0 and $M - 1$. The conversion from bit to integer depends on the mapping. Three types of mapping are cited in [2]: natural, Gray, and anti-Gray. The mapping itself has no effect on the overall code performance, as it is just a different permutation of symbols. However, it is fundamental against the real-environment effects that introduce inter-slot interference (ISI) and memory to the channel. For example, part of the energy of a symbol impulse may leak in the successive one; symbols that have adjacent pulses can risk to be decoded into one another. Therefore, the mapping influences the system performance.
In Tab. 2.3 there is the description of the behaviour of the three mapping, with a PPM order $M = 8$, as described in [2]. Here, in columns two and three,

the least significant bit (LSB) is the further to the right. For this reason, the natural mapping convert integer symbols considering the m binary-sequence of the accumulator output from the left to the right (from the most significant bit (MSB) to the LSB). Instead, Gray and anti-Gray mapping denote the integer symbols considering the accumulator input, respectively ordering the m bits sequences for the minimum Hamming distance (1), and maximal Hamming distance ($\log_2 M$ or $\log_2 M$-1).
Denoting the sequence of m consecutive binary-symbols with $\mathbf{a}^{(\mathrm{m},i)} = \{a_j, a_{j+1}, \ldots, a_{j+m-1}\}$, with $i = 0, \ldots, S-1$ and $j = m \cdot i$, choosing for example the Gray mapping, equation (2.8) gives an idea of the overall APPM block structure.

$$\mathbf{a}^{(\mathrm{m},0)}, \mathbf{a}^{(\mathrm{m},1)}, \mathbf{a}^{(\mathrm{m},2)}, \cdots = \underbrace{100}_{7}, \underbrace{110}_{3}, \underbrace{011}_{5}, \ldots \tag{2.8}$$

Interger symbols of codeword $\mathbf{q} = \{q_0, q_1, \ldots, q_s, \ldots, q_{S-1}\}$ can also be represented as

$$q_s = \sum_{j=0}^{m-1} 2^{m-j-1} \cdot a_j^{(\mathrm{m},i)} \tag{2.9}$$

Laser output is a time-slotted signal where, for each PPM symbols, $M-1$ slot are empty and one is impulsed, as described before. The integer number of the symbols gives the pulse position. PPM frame $\mathbf{c} = \{\mathbf{c}_0, \mathbf{c}_1, \ldots, \mathbf{c}_{S-1}\}$ is composed by S PPM symbols $\mathbf{c}_i$ (the integer pulse position is ignored for simplicity). The $\widehat{k} = 15120$ length has been chosen also for being a multiple of every single value of m; so, for every codeword no leftover symbols will remain.

The real duration of a PPM symbol must also consider the guard time. A common choice is consider the 25% of the PPM symbol duration. Fig. 2.3 shows the overall symbol duration, composed of $M \cdot T_\mathrm{s}$ seconds of slots time plus the guard time.

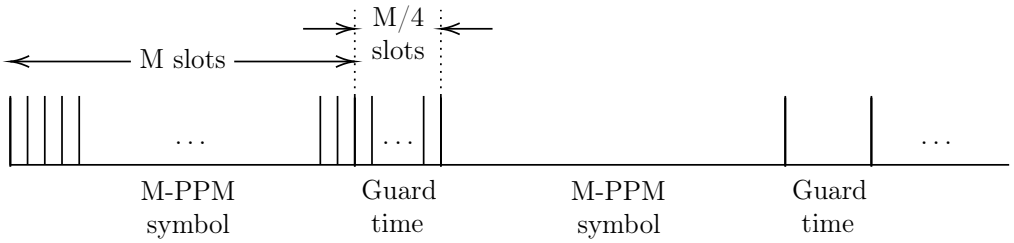

Figure 2.3: Representation of a PPM symbol timing [10].

2.2 Decoder

The decoding system is implemented as an iterative procedure that is very similar to the BCJR decoding concept. This type of decoding allows to understand the single symbol (or bit) error probability, differently from classic decoding algorithms (for example, the Viterbi one) that describe and minimize the word error probability [16]. Considering the modulation and coding technique as a single large encoder, and describing the respective trellis, it is possible to use this type of turbo-iterative demodulator.
This approach, proposed in [2], originates from turbo code applied to the PPM channel and from iterative decoding. Numerical results have been proved that this type of decoding has near-capacity performance, better than the common decoding schemes, as cited in the same paper.

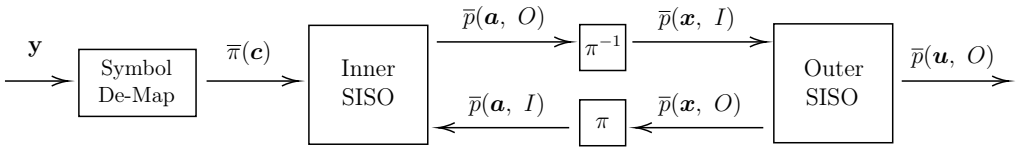

Figure 2.4: SCPPM decoder scheme [2].

In Fig 2.4 is shown the block scheme of the demodulator system: the two soft-input soft-output (SISO) blocks mutually exchange soft information; conceptually they are the same, and are named inner and outer to differentiate the trellis description, respectively for the inner and outer code. Additionally, an interleaver and a de-interleaver connect the flow of information between the SISO blocks, and a symbol de-mapper converts the received

photons in soft information.

In the following sub-sections, in order to describe the decoding algorithm, the soft information is defined as the ratio of two probabilities, in the same way the likelihood ratio of the channel described in equation (1.2). Therefore, the LLR of the generic binary-symbol is defined as

$$\overline{\pi}\left(s_i\right) = \log \frac{p_0\left(s_i\right)}{p_1\left(s_i\right)} \tag{2.10}$$

where $p_0\left(s_i\right)$ and $p_1\left(s_i\right)$ are respectively the probability that s_i is 0 or 1.

2.2.1 Trellis Description

For an easier comprehension of the decoding algorithm, the two SISO trellis information are described. The trellis information consist of a set of states and edges, useful for the decoding process to track down the changes of the encoder states.

The inner trellis is composed by 2 states, 0 and 1, given by the accumulator slot memory. Each state can maintain the same value or change into the other, following the introduction of a new bit. The number of edges for each states is M, considering an input binary-symbol packet $\mathbf{a}^{(\mathrm{m},i)}$. Half of the edges terminate in the 0 state and the other half in the 1 state, as Fig. 2.5 shows.

The outer trellis is composed by 4 states, given by the combination of the 2 bits covolutional code memory slot, but changes its edges configuration based on the rate. For 1/2 and 1/3 code rate, the number of edges per state is 2, while for the 2/3 rate the number increases at 4. This is because of the input bit number: for the former rate, being the input bit only one, the different combinations are 2^1; if the input bits are two, the number of edges increase at 2^2. Fig. 2.6 shows the two outer trellis described.

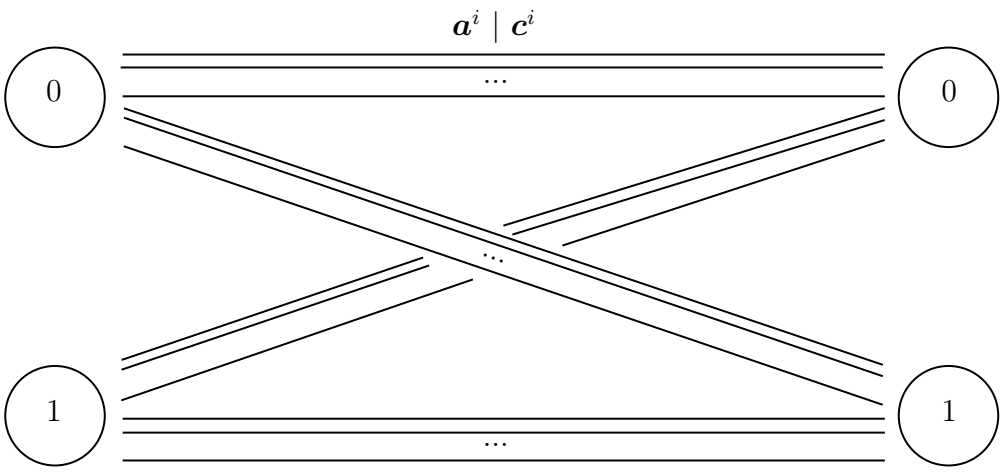

Figure 2.5: Inner trellis description

2.2.2 The max Operation

The $\overset{*}{max}$ function will be used for the calculation of some elements of the decoding algorithm. The definition of this operator is

$$a \overset{*}{max} b \triangleq \log\left(e^a + e^b\right) \tag{2.11}$$

and it has properties like commutativity, associativity, distributive addition; its identity element is $-\infty$, for which $(a)\ \overset{*}{max}(-\infty) = a$.

2.2.3 Decoding Algorithm Description

The inner SISO receives the channel log-likelihoods, described in equation (1.3), and the bit LLRs $\overline{p}(a_{i,j}, \mathcal{I})$ of the codeword $\mathbf{a}$ from the outer SISO. For the first iteration, these are all forced to 0, that means there is no information for any bit of the codeword: in linear scale, the two probabilities in equation (2.10) are equal.
Except for the initial step, the LLRs of the input bits $\mathbf{a}$ are computed as

$$\overline{\pi}\left(\mathbf{a}^{(\mathrm{m},i)}\right) = \sum_{j=0}^{m-1} \frac{1}{2}(-1)^{a_j}\,\overline{p}(a_{i,j}, \mathcal{I}) \tag{2.12}$$

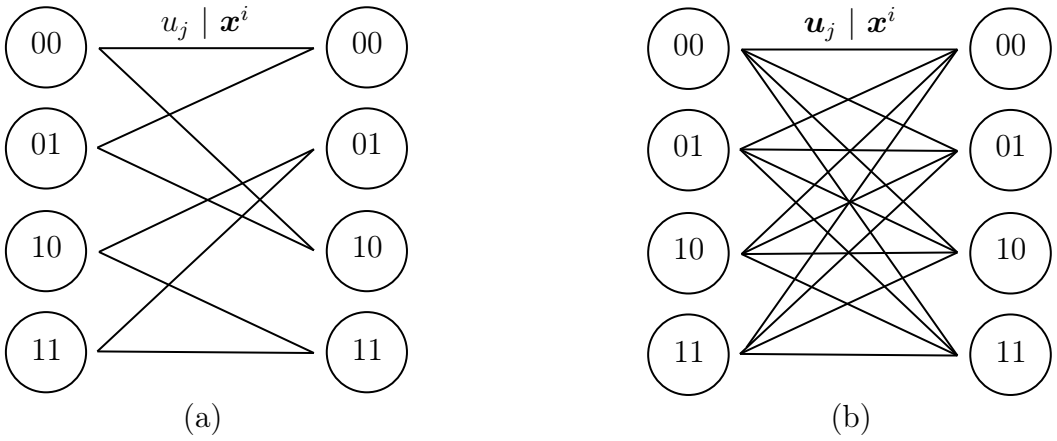

Figure 2.6: Outer trellis description, for 1/2 and 1/3 code rate (a), and 2/3 code rate (b).

for every $i = 0, \ldots, S-1$.

After that, the soft information for the inner trellis edges and states must be computed. Firstly, the information per edge is evaluated for every i as

$$\overline{\gamma}_i(e) = \overline{\pi}\left(\mathbf{a}^{(\mathrm{m},i)}, e\right) + \overline{\pi}(\mathbf{c}_i, e) \tag{2.13}$$

where the specification e means that the channel and **a** bits LLRs must be selected among the correct belonging edge. Equation (2.13) must be computed for every inner edge $2 \cdot M$. Successively, it is necessary to estimate the soft information between the states; equation (2.14) uses the previously described function $\overset{*}{max}$, and applies it to the $\overline{\gamma}_i(e)$

$$\overline{\gamma}_i(s, s') = \overset{*}{max}_{e:\, i(e)=s,\, t(e)=s'}\{\overline{\gamma}_i(e)\}. \tag{2.14}$$

This operation must be done for every couple of initial and terminal trellis state (respectively, s and s'), and for each $i = 0, \ldots, S-1$. Equation (2.14) will produce four $\overset{*}{max}$ operation, each of $M/2$ inputs. For each trellis transitions (for each i), the largest value obtained from equation (2.14) defines the most probable edge.

The likelihood information of the states can be now evaluated. For both the two states, and for each trellis transition i, compute

$$\begin{aligned} \overline{\alpha}_i(s) &= \overset{*}{max}\left(\overline{\alpha}_{i-1}(0) + \overline{\gamma}_{i-1}(0,s), \overline{\alpha}_{i-1}(1) + \overline{\gamma}_{i-1}(1,s)\right) \\ \overline{\beta}_i(s) &= \overset{*}{max}\left(\overline{\beta}_{i+1}(0) + \overline{\gamma}_i(s,0), \overline{\beta}_{i+1}(1) + \overline{\gamma}_i(s,1)\right) \end{aligned} \tag{2.15}$$

initializing the state information as

$$\begin{aligned} \overline{\alpha}_0(s) &= \begin{cases} 0, & \text{s} = 0 \\ -\infty, & \text{otherwise} \end{cases} \\ \overline{\beta}_{S-1}(s) &= 0 \end{aligned} \tag{2.16}$$

The values in vector $\overline{\boldsymbol{\alpha}}(s)$ give the most probable initial state considering each trellis transition; the initialization imply that all the states different from the 0 state are totally improbable, that means the initial state for the first transition is certainly the 0 state. Vector $\overline{\boldsymbol{\beta}}(s')$ has the same meaning of $\overline{\boldsymbol{\alpha}}(s)$, but refers to the final state for each transition. The initialization in equation (2.16) imply that the final state of the final transition is equiprobable, and so there is no constraint.
In equation (2.15), the $\overset{*}{max}$ operation takes two inputs given by the combination of an edge and a state.

Computing

$$\overline{\lambda}_i(e) = \overline{\alpha}_{i-1}(i(e)) + \overline{\gamma}_i(e) + \overline{\beta}_i(t(e)) \tag{2.17}$$

for every edge and trellis transition, an element that include all the information about initial and terminal states and trellis edges has been obtained. For every transition i, the largest element specifies the most probable initial state, terminal state, and so the edge connecting them. Therefore, for every iteration of the decoding algorithm, and for every decoded codeword, $\overline{\lambda}_i(e)$ indicate all the transitions and so the codeword $\mathbf{a}$ itself.

The inner SISO finally produces the output bit LLRs of codeword $\mathbf{a}$ as

$$\overline{p}\left(a_{i,j},\mathcal{O}\right)=\overset{*}{max}_{e\in\mathcal{E}_{0,j}^{A}}\{\overline{\lambda}_{i}\left(e\right)\}-\overset{*}{max}_{e\in\mathcal{E}_{1,j}^{A}}\{\overline{\lambda}_{i}\left(e\right)\}-\overline{p}\left(a_{i,j},\mathcal{I}\right) \tag{2.18}$$

where $e\in\mathcal{E}_{0,j}^{A}$ indicates all the edges e included in the edge set $\mathcal{E}$ with $a\left(e\right)_{j}=0$ (the same for $e\in\mathcal{E}_{1,j}^{A}$ but with $a\left(e\right)_{j}=1$). This operation has to be done for every transition i, and for every $j=0,\ldots,M-1$. The $\overset{*}{max}$ operations have M inputs.

The LLRs thus found must be de-interleaved; this repeats the same procedure of the interleaver, with a different quadratic polynomials obtained by the inversion of equation (2.6)

$$\pi^{-1}\left(j\right)=\left(14891j+210j^{2}\right)\bmod 15120\,. \tag{2.19}$$

The inner SISO has the same procedure, but with a different description of the trellis. This block receives the LLRs $\overline{p}\left(x_{i,j},\mathcal{I}\right)$ from the de-interleaver, and computes the edge output symbol log-likelihoods

$$\overline{\pi}\left(\mathbf{x}^{i}\right)=\sum_{j=1}^{r}\frac{1}{2}\left(-1\right)^{x_{i,j}}\overline{p}\left(x_{i,j},\mathcal{I}\right) \tag{2.20}$$

for each of the four states of the outer trellis, and for each $i=0,\ldots,k^{*}-1$, where k^{*} depends on the chosen code rate, as specified in Tab. 2.2. The sum upper limit r also depends on the chosen code rate, being 2 or 3 the number of output bits.

The outer SISO then set

$$\overline{\gamma}_{i}\left(e\right)=\overline{\pi}\left(\mathbf{x}^{i},e\right) \tag{2.21}$$

for each edges of the outer trellis and for each i. The term $\overline{\pi}\left(u_{j},\mathcal{I}\right)$, that describes the LLRs of the encoder input binary-symbols, is always equal to 0 for the equi-probability hypothesis.

Similarly to the inner trellis, the initial and terminal state information must be evaluated by initializing

$$\begin{aligned} \overline{\alpha}_0(s) &= \begin{cases} 0, & \mathrm{s} = 0 \\ -\infty, & \text{otherwise} \end{cases} \\ \overline{\beta}_{k^*-1}(s) &= \begin{cases} 0, & \mathrm{s} = 0 \\ -\infty, & \text{otherwise} \end{cases} \end{aligned} \tag{2.22}$$

and recursively computing

$$\begin{aligned} \overline{\alpha}_i(s) &= \overset{*}{max}_{e:\, t(e)=s}\{\overline{\alpha}_{i-1}(i(e)) + \overline{\gamma}_{i-1}(e)\} \\ \overline{\beta}_i(s) &= \overset{*}{max}_{e:\, i(e)=s}\{\overline{\beta}_{i+1}(t(e)) + \overline{\gamma}_i(e)\} \end{aligned} \tag{2.23}$$

for every state and transition i.

The global information can be evaluated as

$$\overline{\lambda}_i(e) = \overline{\alpha}_{i-1}(i(e)) + \overline{\lambda}_i(e) + \overline{\beta}_i(t(e)) \tag{2.24}$$

for each edges e and transition i.

Finally, it is possible to compute the LLRs of the user data $\mathbf{u}$, and of the vector $\mathbf{x}$ that will be send to the inner SISO in order to start a new iteration, if needed. Respectively

$$\overline{p}(u_{i,j}, \mathcal{O}) = \overset{*}{max}_{e \in \mathcal{E}^U_{0,j}}\{\overline{\lambda}_i(e)\} - \overset{*}{max}_{e \in \mathcal{E}^U_{1,j}}\{\overline{\lambda}_i(e)\} \tag{2.25}$$

$$\overline{p}(x_{i,j}, \mathcal{O}) = \overset{*}{max}_{e \in \mathcal{E}^X_{0,j}}\{\overline{\lambda}_i(e)\} - \overset{*}{max}_{e \in \mathcal{E}^X_{1,j}}\{\overline{\lambda}_i(e)\} - \overline{p}(x_{i,j}, \mathcal{I}) \tag{2.26}$$

for every trellis transition i, and every binary symbol j.

At this point, the stopping-criterion must be checked: if it is satisfied, it is possible to stop the decoding algorithm, as a codeword has been obtained; otherwise, another decoding iteration must be done, interleaving the encoder

output LLRs $\overline{p}\left(x_{i,j}, \mathcal{O}\right)$ and sending them to the inner SISO.

2.3 Simulations and Results

The entire SCPPM encoding and decoding scheme has been implemented in C++ language. The code allows the simulation of the performance graphs. Initially, with the same input data described in [2] for a specific graph, the correct functioning of the algorithm has been tested, matching the resulting curve with the theoretic one. In order to obtain a performance graph, the simulation implements a Montecarlo algorithm.

As inputs, the simulator takes:

- the Montecarlo information (maximum and minimum number of iterations, maximum number of errors as a stopping criterion);
- the PPM order and the type of mapping;
- convolutional code information (number of input and output bits, number of memory stages, and polynomial generator);
- the number of decoding iteration;
- the mean noise photon flux, n_b in phe/slot, the number and the values of the mean signal photon flux, n_s in phe/slot, to be tested.

Some precautions have been taken in order to increase the simulation speed. Considering the time needed for a single decoding iteration, Tab. 2.4 shows the modifies that have been produced for speed improvement.
The speed gain from the Matlab implementation to the C++ launch on a server is 9.6478 ms. The function $\overset{*}{max}$ was critical, because of the large number of times it must be launched. The implementation of a simplified version of this function made the simulator much faster. The LUT version of the $\overset{*}{max}$ made the simulator about 2.5 times faster than previously. Eventually, a fixed point version of the program, along with a compiler option, have been implemented. These values have been measured with a $M = 64$,

Optimizations	Time per decoding iteration, [ms]
Matlab script	9.669
$\overset{*}{max}$ simplified	0.2156
$\overset{*}{max}$ Lut	0.0852
-O3 opt.	0.0486
Fixed point impl.	0.0237
Server	0.0212

Table 2.4: Improvements in SCPPM decoding times.

$T_s = 16$, $R = 1/2$ code, with 50 maximum number of decoding iterations, and a $n_b = 0.2$ phe/slot. The n_s value has been always set very small, so that the simulator was not ever able to decode the frame. In this way, it was possible to obtain a more precise evaluation of the mean time per decoding iteration.

In Fig 2.7 is shown an example of a performance graphs, obtained with the C++ implementation of the iterative SCPPM decoding algorithm. Black, red, and blue curves represent respectively a 1/2, a 1/3, and a 2/3 code rate. The different symbols represent the different PPM order values. For all the curves showed, a $T_s = 16$ ns, a $n_b = 0.2$ phe/slot, and a Gray mapping are imposed. Every curve in the graph represents the frame error rate (FER) achievable with a given value of n_s in dB phe/ns, for the previous described parameters. The FER is the ratio between the transmitted frames which present at least one incorrect bit, and the totality of the transmitted frames (i.e., the totality of the Montecarlo iterations). The simulation implemented can produce different curves, for a single combination of parameters, only changing the maximum number of decoding iterations. From 5 to 50, it has been observed that beyond 25 maximum decoding iteration per codeword there is no performance gain. So, this number is the right trade-off between the decoding speed and quality. With less iterations, the algorithm is faster but produces performance curves not steeper as the ones showed in Fig 2.7.

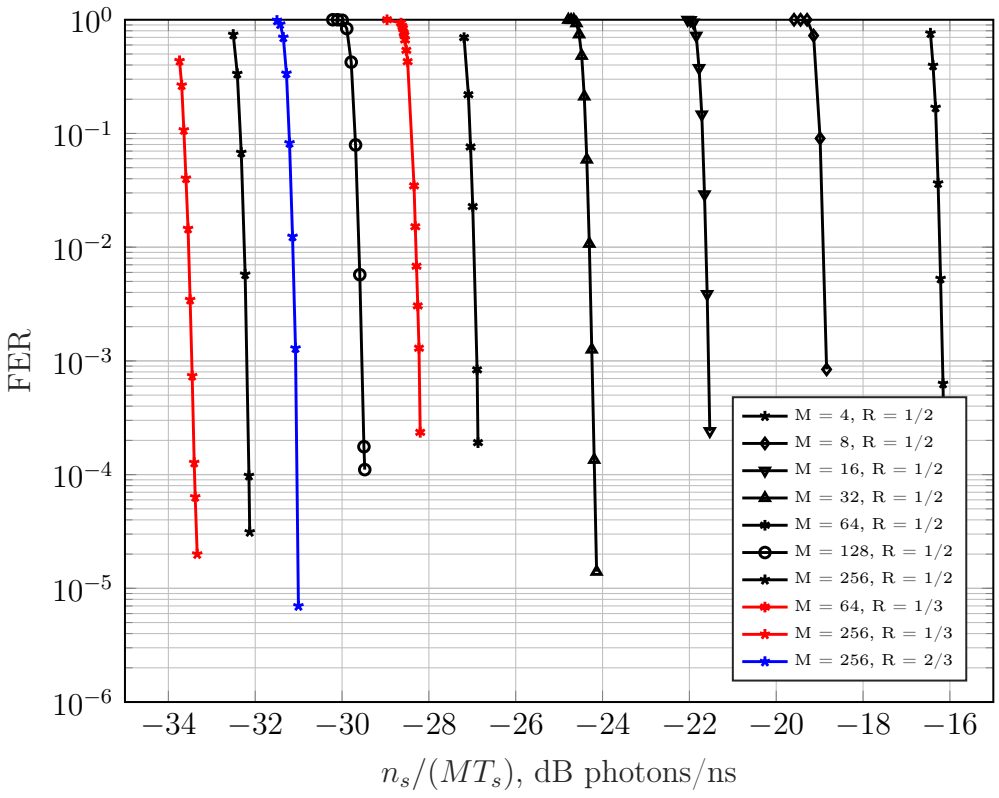

Figure 2.7: SCPPM performance graph, 25 maximum decoding iterations.

Chapter 3

Link Budget

Performing the analysis of an optical link budget for system optimization involves considering the most suitable configuration of a certain number of parameters, fulfilling the constraints imposed by technology. This configuration must produce the best possible system performance, satisfying some specific targets imposed by the user. It has also to consider all potential changes during the operation time.
A possible approach to an optical link budget can be found in [6, 9], and the following sections heavily rely on these documents. However, it is necessary to consider that their power budget has been applied to an optical communication link between a satellite orbiting around Mars and an Earth ground receiver. For this reason, some differences are introduced in this thesis, where the focus is on relaying systems.

Fig. 3.1 describes the method that has been used for the optical link budget. Red-coloured blocks portray the target requirements imposed by the user, that represent the goal performance of the system: B_{r}^{*} is the target information data rate, in Mbit/s; P_{e}^{*} is the maximum tolerable FER; $\mathcal{M}^{*}$ is the target link margin that represents the minimum desired difference between the number of signal photons per second received from the transmitting unit, n_{s} in phe/s, and the minimum number of signal photons per second that satisfies the FER requirement, $n_{\mathrm{s,min}}$ in phe/s.

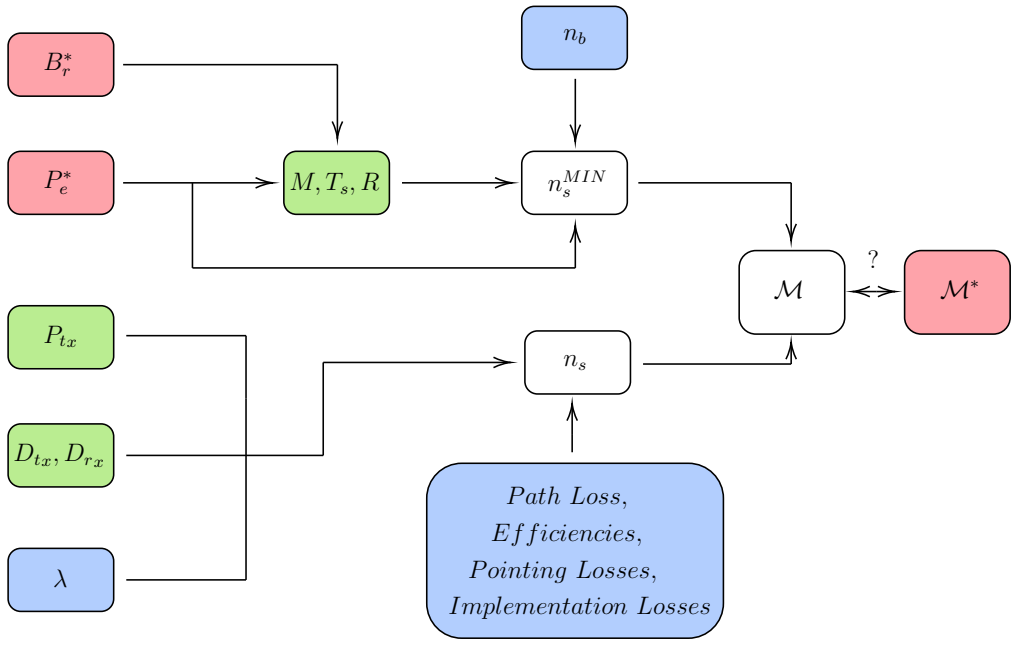

Figure 3.1: Flow chart of the optical link budget.

Green-coloured blocks represent the tunable parameters: P_{tx} is the mean laser power, in W; D_{tx} and D_{rx} are respectively the transmitting and receiving antenna diameters, in m; M is the PPM order; T_{s} is the time slot, in ns, while R is the convolutional code rate. These last three parameters are also denoted as modulation and coding parameters, being directly connected to the transmission system described in chapter 2. The values of the green-coloured parameters can be modified and adjusted in order to change n_{s} and $n_{\text{s,min}}$ and satisfy the requirements.
Finally, the blue-coloured blocks represent the "input" parameters that must be considered as fixed: λ is the laser wavelength in nm; n_{b} is the mean number of noise photons per second at the receiving system, in phe/s; efficiencies, pointing, implementation and path losses, can also be considered fixed; pointing losses will be better explained in section 3.1, while the others have been explained in section 1.3. Here, η_{tx}, η_{rx} and $L_{\text{det,impl}}$ consider all the non-idealities described in the cited section, respectively for transmitting and receiving antennas and for detection and implementation losses. Space losses are variable during the mission, for the motion of the two planets and

satellites; for each of the four planets we will consider a worst distance value. Space losses are described in section 1.3.

Once the requirements and the fixed parameters are given, the other system parameters can be tuned; the arrows in Fig. 3.1 help to understand the logical flow of the link budget method. Starting from the target P_{e}^{*} and the target B_{r}^{*}, it is possible to find a combination of M, T_{s} and R for a data rate

$$B_{\mathrm{r}} = \frac{15120\,R - N_{\mathrm{extra}}}{T_{\mathrm{F}}} = \frac{15120\,R - N_{\mathrm{extra}}}{MT_{\mathrm{s}}\,(15120/\log_2 M)\,\alpha_{\mathrm{gt}}}. \tag{3.1}$$

Here, B_{r} is calculated from the ratio between the number of information bits and the frame time, denoted as T_{F}. The former is obtained considering the number of frame bits (15120, as described in chapter 2), the convolutional code rate, and a fixed parameter N_{extra}, that considers the CRC and the termination bits; T_{F}, instead, is a measure of the frame time in the channel: it considers the number of slots per symbols M, the slot time T_{s}, the number of symbols in a PPM frame and the guard time parameter α_{gt}. The expression $\log_2 M$ is equal to m, the number of bits per PPM symbol, as previously explained in chapter 2. Finally, α_{gt} is greater than one: for example, if the guard time is fixed at 25%, its value will be equal to 1.25.
With the modulation and coding parameters determined, it is possible to obtain the value of $n_{\mathrm{s,min}}$ from the performance graphs and the FER requirement. Here, n_{b} must be taken into account, as it plays a fundamental role in the determination of the curve to be used, being

$$n_{\mathrm{s}}^{slot} = n_{\mathrm{b}} \cdot T_{\mathrm{s}}\,. \tag{3.2}$$

Equation (3.2) shows the relationship between n_{b} and the mean number of noise photons per slot, n_{s}^{slot} in phe/slot, used in the PPM channel. In the following link budgets, the former, also denoted as mean noise flux, is

considered a fixed value. Actually, it can be expressed as [1]

$$n_{\mathrm{b}} = [L_{\mathrm{sky,planet,stray}} \Omega_{\mathrm{FOV}} A_{\mathrm{rx}} \Delta\lambda + UnExtLaserSignal] \cdot \\ \cdot \eta_{\mathrm{DetEff}} \frac{\lambda}{hc} + DarkCounts\,. \tag{3.3}$$

We see that the mean noise flux depends on various effect; *DarkCounts* represents the detector dark noise and η_{DetEff} the detector efficiency; *UnExtLaserSignal* is the residual laser power remaining into the band when there is no transmission beam; $\Delta\lambda$ depends on the detector spectral filter, while $\Omega_{\mathrm{FOV}} A_{\mathrm{rx}}$ stands for the receiving aperture area. Finally, $L_{\mathrm{sky,planet,stray}}$ represents the radiation received at the detector that is not the transmitted beam. Here, these relations are not considered and n_{b} has a fixed value, taken from table 8 in [6].

The number of signal photons per second, n_{s}, is given by [1, 6, 9, 10]

$$n_{\mathrm{s}} = EIRP \cdot G_{\mathrm{rx}} \cdot \eta_{\mathrm{rx}} \cdot L_{\mathrm{space}} \cdot \frac{\lambda}{hc} \tag{3.4}$$

with

$$EIRP = P_{\mathrm{av}} \cdot G_{\mathrm{tx}} \cdot \eta_{\mathrm{tx}} \cdot L_{\mathrm{pointing}} \tag{3.5}$$

where η_{tx}, η_{rx}, L_{pointing}, and L_{space} are respectively the transmitting and receiving efficiencies, the pointing and space losses, and h is the Planck constant. The antenna gains are

$$\begin{aligned} G_{\mathrm{tx}} &= \left(\frac{\pi D_{\mathrm{tx}}}{\lambda}\right)^2 \\ G_{\mathrm{rx}} &= \left(\frac{\pi D_{\mathrm{rx}}}{\lambda}\right)^2 \end{aligned} \tag{3.6}$$

and depend on the aperture diameters and on λ. Equations (3.6) specify the maximum on-axis gain, differently from equations (1.5) and (1.6) that also explicit the efficiency losses; as regards the power budget, transmitting

and receiving gains are taken as their maximum value, and efficiencies are calculated separately, as described in equation (3.4) and in equation (3.5). P_{av} represents the mean power pulse of the single PPM symbol. This value derives from the peak laser power of the laser transmitter, averaged over the number of slots in a PPM symbol, also considering the time guard

$$P_{\mathrm{av}} = \frac{P_{\mathrm{pk}}}{M\,\alpha_{\mathrm{gt}}}\,. \tag{3.7}$$

Finally, the residual link margin is calculated as

$$\mathcal{M} = n_{\mathrm{s}} - n_{\mathrm{s,min}}. \tag{3.8}$$

If the value is negative or less than the requirement, it is necessary to change and adjust some parameters, even at the price of reducing the data rate B_{r}.

3.1 Pointing

In section 1.4 pointing losses are illustrated as the only random variable in the context of the power budget, originated mostly by the random mechanical noise of the platform. Distances, sun-probe-earth (SPE) and sun-earth-probe (SEP) angles are variable quantities during the mission, but they can be calculated very precisely. For these reasons, the outage probability described in section 1.4 depends only on pointing.

The procedure adopted for the power budget between the two satellite platforms consist in imposing a fixed σ_θ parameter and an outage probability target, choosing between the Gaussian beam model and the circular aperture approximation model. With these inputs, and with the use of the bisection algorithm, the optimal gain and the relative effective gain can be found. Algorithm 3 explains the various steps for obtaining the optimal value of the antenna gains. This method can work with the hypothesis of equal antennas. In Fig. 3.2 it is shown the result of this procedure for two different values of σ_θ, for the two different pointing models, and for a fixed P^*_{out} of 5%. Impos-

Algorithm 3: Numerically derive the optimum antenna gains from pointing information

Result: Optimal gain G_{opt}, effective gain G_{eff};

Input: σ_θ for the Rayleigh distribution, outage probability target P^*_{out}, type of pointing model (imposing the parameter α);

1) Produce a gain axis values G, in dB;
2) For every value of the antenna gain, launch the bisection algorithm with the input described; it will numerically find the value of K from equation (1.19), where:
   - $\alpha = 1$, Gaussian beam model;
   - $\alpha = 0.188$, circular aperture approximation model;
3) Impose the equation

$$G_{\text{eff}} = \log_{10} e^{-K} + G \tag{3.9}$$

   for every value of G and K previously found;
4) Find the value of G_{opt} for which G_{eff} is maximized.

ing a more precise pointing technology, it is clear that antennas can obtain an increase in gain, because the narrower beam is very precisely directed towards the receiver. Moreover, for the same σ_θ, the optimal gain calculated with the Gaussian beam model will be smaller than the one obtained with the circular aperture approach, being the former a worst-case approach.

Once the antenna gain value G_{opt} for which the effective gain G_{eff} result maximum has been found, pointing losses can be calculated from the difference between the effective antenna gain without losses and the effective antenna gain obtained from the input parameters. This derive directly from equation (3.9) described in point 3) in algorithm 3. Here, G stands for the effective antenna gain without pointing losses, while the logarithm is from equation (1.11).

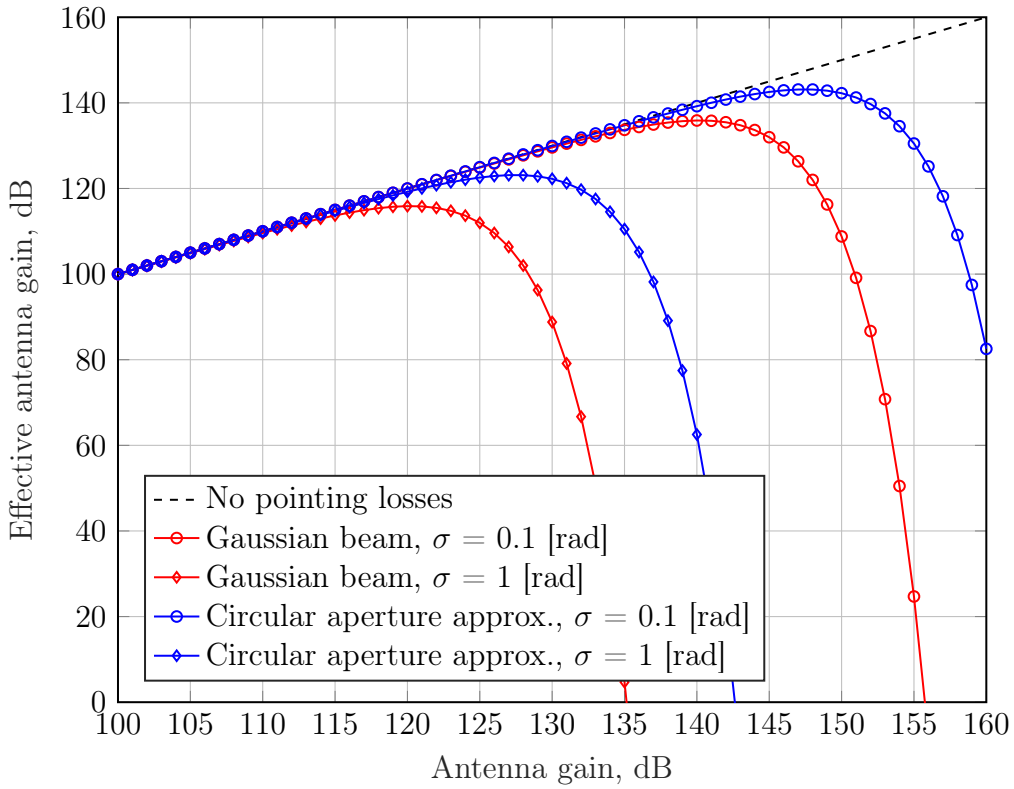

Figure 3.2: Effective gain found with algorithm 3.

Once the optimal gain is calculated, it is possible to find the antenna diameters from equation (3.6), imposing λ; then we can continue the link budget steps as previously described.
This way, the antenna diameters are not variable anymore, but this method permits to find the right value of their dimension to optimize the far-field gain with respect to the pointing losses.

3.2 Downlink Budget

This section describes the link budgets performed for the four planets. All the following tables display a worst case column that refers to the case the spacecraft is in the farther position respect to the receiving unit. Moreover,

the data column is subdivided into three parts: the central one reports the linear value of the respective parameter, with the units at its right; the left sub-column represents dB values.

Tab. 3.1 shows a downlink budget from Mars imposing a σ_θ equal to $1\,\mu rad$. Under the caption *Signaling and Fixed Parameter* all the parameters needed to the transmission modulation are listed. PPM order, convolutional code rate and slot time, along with the information of the mean noise flux, are the parameters needed for the selection of the performance graph. The mean noise flux, in phe/ns, and the mean noise flux per slot, in phe/slot, are respectively n_b and n_b^{slot} described in equation (3.2). The mean noise flux per slot changes when varying the slot time. The guard time and the outage probability are fixed parameters imposed respectively to 25% and 5%. The $\sigma_\theta^{\mathrm{Max}}$ entry specifies its value and the model used to calculate the G_{opt} and the pointing losses.

Laser Transmitter section gives information about the wavelength and the mean power employed in the link: λ equal to 1064 nm is a very common choice, as explained previously in section 1.2.1, while imposing 5 W of mean laser power is specified in the *RECOMMENDATION ITU-R SA.1742*. The peak laser power, then, is calculated from equation (3.7).

Section *Deep Space Orbiter* and *Near Earth Orbiter* describe gains and diameters respectively for the transmitting and the receiving antenna. The method to obtain these parameters from σ_θ and P^*_{out} is given in paragraph 3.1. The efficiencies are fixed at a realistic value of -5 dB, and they consider all the non-ideality cited in section 1.3. The -5 dB is a value taken from table 8 in [6]. The pointing losses are obtained once the G_{eff} and G_{opt} have been calculated, as previously described.

Section *Distance Range* describes the distance, in AU, between the two unit, and the space losses calculated with equation (1.7).
Section *Other* specifies the detection and implementation losses described in

paragraph 1.3.

Finally, under *Link Performance* are listed the requirements and the performance that the system can achieve. Average received power and photon flux are two different ways to express n_s, respectively in dBW, phe/ns and dB phe/ns. The last unit of measurements is the same of the performance graph shown in Fig. 2.7. Minimum average received power and photon flux instead represent $n_{s,min}$ obtained from the signal parameters. Link margin, FER target and the information data rate are, respectively, the residual dB calculated from equation (3.8), the target maximum frame error, and the data rate achieved with the described configuration as calculated from equation (3.1).

For the power budget described in Tab. 3.1, imposing a σ_θ equal to $1\,\mu rad$, the resulting antenna gains and diameters are respectively 127 dB and 0.76 m. The total pointing losses are -3.88 dB for both the antennas. The worst case distance of 2.68 AU results in -373.49 dB of space losses. Considering all the parameters of equations (3.4) and (3.5), a -35.98 dB phe/ns average received signal photon flux has been obtained. In order to satisfy a positive link margin, a PPM order of 128, along with a 1/3 code rate and a 256 ns slot time, have been chosen. This choice produces a minimum average received photon flux of -38.37 dB phe/ns, achieving a 2.39 dB link margin and a 0.06 Mb/s data rate.
The same procedure has been performed for the $\sigma_\theta = 0.75\,\mu rad$; smaller σ_θ enhances the antenna gains and diameters, making the n_s higher, respectively 130 dB, 1.07 m, and -30.93 dB phe/ns. Choosing the G_{opt} here has been demonstrated a correct procedure: even if the pointing losses are bigger than the previous case (-4.357 dB for each antenna), a better mean received photon flux have been obtained. Choosing the same modulation and coding parameter leads to a link margin of 7.44 dB. It also possible to gain in data rate, reducing the PPM order (up to the last value for which the link margin is positive). For example, with $M = 64$, a 0.097 Mb/s date rate can be achieved along with a 4.83 dB link margin.

Link Parameter	dB	**Worst** Linear	Units
Signaling and Fixed Parameter			
PPM Order		128	
Convolutional Code Rate		1/3	
Slot Time		256	ns
Guard Time		25	%
Mean Noise Flux	-19.17	1.21e-02	phe/ns
Mean Noise Flux per slot		3.10	phe/slot
Outage Probability		5	%
σ_θ^{Max} of the tracking error loop, Circ. ap. approx.		1	μrad
Laser Transmitter			
Average Laser Power	6.99	5	W
Peak Laser Power	29.03	800	W
Wavelength		1064	nm
Deep Space Orbiter			
Far-Field Antenna Gain	127.00	0.76	m
Transmitter Efficiency	-5.00		
Pointing Losses	-3.88		
Distance Range			
Space Loss	-373.49	2.68	AU
Near Earth Orbiter			
Receiver Gain	127.00	0.76	m
Receiver Efficiency	-5.00		
Pointing Losses	-3.88		
Other			
Detection/Implementation Losses	-3.00		
Link Performance			
Average Received Power	-133.27		W
Average Received Photon Flux	-35.98	2.52e-04	phe/ns
Minimum Average Received Power	-135.66		W
Minimum Average Received Photon Flux	-38.37	1.46e-04	phe/ns
Link Margin	2.39		
FER target		1.00e-04	
Information Data Rate		0.06	Mb/s

Table 3.1: Mars link budget.

In Tab. 3.2 is shown the link budget performed for the spacecraft in orbit around Venus. With the outage probability and σ_θ being equal to the previous link budget, the same antenna gains and pointing losses are obtained. However, the average received photon flux is larger than the previous case, because of the smaller distance. For this reason, a 32 PPM order can be chosen, maintaining a positive link budget and enhancing the information data rate, at the same time. Moreover, a smaller peak laser power is requested.

Tab. 3.3 and 3.4 report respectively the link budget for Uranus and Neptune. These are the most critical budget because of the huge distance of the satellites. With the same parameters imposed in the previously two examples, no modulation and coding configuration satisfies a positive link margin. For these two planets is requested a more tightening pointing, in order to enhance the antenna gains, and an higher laser power. Therefore, the last two communication links will be possible only if the technology will satisfies more stringent power and pointing requirements.

Tab. 3.5 describes the maximum reachable distances in AU, given a particular configuration of all the parameters. Using the Gaussian method to find the optimum gain, a code rate $R = 1/3$, a slot time $T_\mathrm{s} = 256\,ns$ and an outage probability $P_\mathrm{out} = 5\%$, it is possible to choose the PPM order and the $\sigma_{\theta,\mathrm{max}}$ in order to satisfy the maximum distance between the satellites and the relay. This method can work only if the peak laser power is fixed. Here, a $P_\mathrm{pk} = 500\,W$ is imposed, as suggested by ESA information. It is clear that imposing a more stringent pointing error achieves a bigger antenna gains, and so it can be possible for the beam to reach larger distances. Moreover, decreasing the PPM order has the same effect; however, the average laser power spent for the signal transmission increases.

Finally, in Fig. 3.3 are shown all the $n_{\mathrm{s,min}}$ values relative to FER $= 10^{-4}$. In the ordinate axis there are also shown the information data rates achievable for every curve, obtained with equation (3.1). It is clear that increasing T_s or the PPM order M have the effect of reducing the data rate

Link Parameter	dB	**Worst** Linear	Units
Signaling and Fixed Parameter			
PPM Order		32	
Convolutional Code Rate		1/3	
Slot Time		256	ns
Guard Time		25	%
Mean Noise Flux	-19.17	1.21e-02	phe/ns
Mean Noise Flux per slot		3.10	phe/slot
Outage Probability		5	%
σ_θ^{Max} of the tracking error loop, Circ. ap. approx.		1	μrad
Laser Transmitter			
Average Laser Power	6.99	5	W
Peak Laser Power	23.01	200	W
Wavelength		1064	nm
Deep Space Orbiter			
Far-Field Antenna Gain	127.00	0.76	m
Transmitter Efficiency	-5.00		
Pointing Losses	-3.88		
Distance Range			
Space Loss	-369.73	1.74	AU
Near Earth Orbiter			
Receiver Gain	127.00	0.76	m
Receiver Efficiency	-5.00		
Pointing Losses	-3.88		
Other			
Detection/Implementation Losses	-3.00		
Link Performance			
Average Received Power	-129.51		W
Average Received Photon Flux	-32.22	6.00e-04	phe/ns
Minimum Average Received Power	-130.44		W
Minimum Average Received Photon Flux	-33.15	4.84e-04	phe/ns
Link Margin	0.93		
FER target		1.00e-04	
Information Data Rate		0.16	Mb/s

Table 3.2: Venus link budget.

Link Parameter	dB	**Worst** Linear	Units
Signaling and Fixed Parameter			
PPM Order		256	
Convolutional Code Rate		1/3	
Slot Time		256	ns
Guard Time		25	%
Mean Noise Flux	-19.17	1.21e-02	phe/ns
Mean Noise Flux per slot		3.10	phe/slot
Outage Probability		5	%
σ_θ^{Max} of the tracking error loop, Circ. ap. approx.		1	μrad
Laser Transmitter			
Average Laser Power	20.97	125.00	W
Peak Laser Power	46.02	40	kW
Wavelength		1064	nm
Deep Space Orbiter			
Far-Field Antenna Gain	127.00	0.76	m
Transmitter Efficiency	-5.00		
Pointing Losses	-3.88		
Distance Range			
Space Loss	-391.43	21.09	AU
Near Earth Orbiter			
Receiver Gain	127.00	0.76	m
Receiver Efficiency	-5.00		
Pointing Losses	-3.88		
Other			
Detection/Implementation Losses	-3.00		
Link Performance			
Average Received Power	-137.22		W
Average Received Photon Flux	-39.93	1.02e-04	phe/ns
Minimum Average Received Power	-138.27		W
Minimum Average Received Photon Flux	-40.98	7.98e-05	phe/ns
Link Margin	1.05		
FER target		1.00e-04	
Information Data Rate		0.03	Mb/s

Table 3.3: Uranus link budget.

Link Parameter	dB	**Worst** Linear	Units
Signaling and Fixed Parameter			
PPM Order		256	
Convolutional Code Rate		1/3	
Slot Time		256	ns
Guard Time		25	%
Mean Noise Flux	-19.17	1.21e-02	phe/ns
Mean Noise Flux per slot		3.10	phe/slot
Outage Probability		5	%
σ_θ^{Max} of the tracking error loop, Circ. ap. approx.		1	μrad
Laser Transmitter			
Average Laser Power	23.98	250	W
Peak Laser Power	49.03	80	kW
Wavelength		1064	nm
Deep Space Orbiter			
Far-Field Antenna Gain	127.00	0.76	m
Transmitter Efficiency	-5.00		
Pointing Losses	-3.88		
Distance Range			
Space Loss	-394.86	31.33	AU
Near Earth Orbiter			
Receiver Gain	127.00	0.76	m
Receiver Efficiency	-5.00		
Pointing Losses	-3.88		
Other			
Detection/Implementation Losses	-3.00		
Link Performance			
Average Received Power	-137.65		W
Average Received Photon Flux	-40.36	9.20e-05	phe/ns
Minimum Average Received Power	-138.27		W
Minimum Average Received Photon Flux	-40.98	7.98e-05	phe/ns
Link Margin	0.62		
FER target		1.00e-04	
Information Data Rate		0.03	Mb/s

Table 3.4: Neptune link budget.

$\sigma_{\theta,max}$ [μrad]	PPM Order | Average Laser Power [W]						
	256|1.56	128|3.12	64|6.25	32|12.50	16|25	8|50	4|100
1.00	0.252	0.264	0.276	0.289	0.302	0.317	0.332
0.50	1.007	1.055	1.104	1.156	1.210	1.268	1.328
0.10	25.183	26.371	27.615	28.917	30.246	31.709	33.205
Data Rate, [kb/s]	32.33	56.58	97.00	161.66	258.66	387.99	517.32

Table 3.5: Maximum reachable distances, in AU, with a given PPM order and a specified $\sigma_{\theta,max}$. Results have been found using Gaussian method, $R = 1/3$, $T_s = 256\,ns$, and $P_{out} = 5\%$. Peak Laser Power fixed at 500 W.

and the minimum average signal photon flux per second. In this way, it is possible to improve the stability of the system, increasing the residual link margin for the received n_s. The same effect can be achieved by reducing the code rate R.

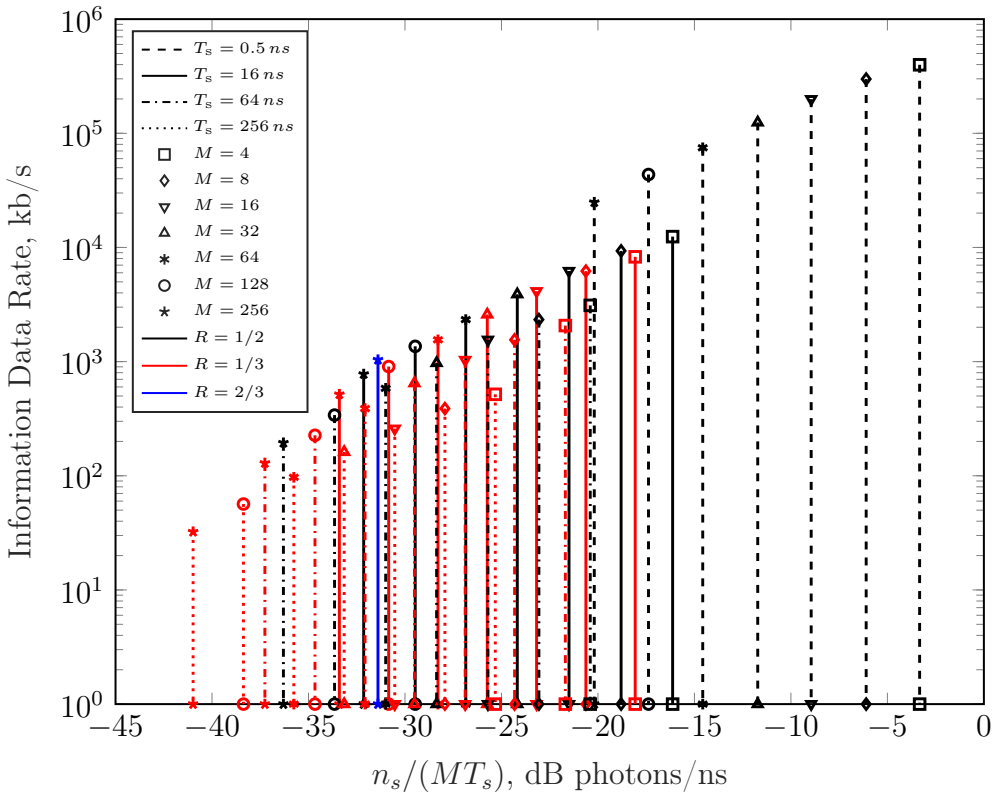

Figure 3.3: Data rate and $n_{\mathrm{s,min}}$ for all the performance graphs obtained, imposing a FER = 10^{-4}.

Chapter 4

LDPC

In this chapter another type of code will be described and compared with the SCPPM method. The binary low-density parity-check (LDPC) codes are categorized as linear block code and they are specified as a possible implementation by the CCSDS standard for telemetry. Therefore, it is interesting to apply LDPC coding, with the related iterative decoding algorithm, to the optical deep-space links previously described. In regard to the SCPPM coding and decoding approach, the LDPC performances is expected to be worse. However, the decoding algorithm is simpler and easier to implement on the spacecraft.

4.1 Encoder

LDPC codes are described by $\mathbf{G}_{k\times n}$ and $\mathbf{H}_{(n-k)\times n}$, respectively denominated the code-generator matrix and the parity matrix. The number of input bits is commonly represented by k, the number of codeword bits by n, and the code rate is defined as $R = k/n$. For linear codes, the codeword $\mathbf{c}$ corresponding to a binary message $\mathbf{u}$ is given by

$$\mathbf{c} = \mathbf{u} \cdot \mathbf{G}. \tag{4.1}$$

For this implementation, systematic encoder must be considered, because their construction is simpler. Therefore, the generator matrix can be defined as $\mathbf{G} = \left[\mathbf{I}_k | \mathbf{W}_{k\times(n-k)}\right]$, where $\mathbf{I}_k$ is an identity matrix, and $\mathbf{W}_{k\times(n-k)}$ will be defined later. The binary-check matrix imposes that $\mathbf{c} \cdot \mathbf{H}^T = \mathbf{0}_{1\times(n-k)}$, for every codeword that belongs to the code. In fact, among the 2^n possible codeword combination, only 2^k are valid.

LDPC codes can be described by a Tanner graph, which is a bipartite graph with n variable nodes (VNs) and $n-k$ check nodes (CNs). Every CN represents a single parity-check constraints. A VN i is connected to a CN j if the parity matrix element $h_{j,i} = 1$. In Fig. 4.1 is shown a simplified version

$$H = \begin{array}{c} \begin{matrix} V_n^1 & V_n^2 & V_n^3 & V_n^4 & V_n^5 & V_n^6 \end{matrix} \\ \begin{bmatrix} 1 & 0 & 1 & 1 & 0 & 0 \\ 1 & 1 & 0 & 0 & 1 & 0 \\ 0 & 1 & 1 & 0 & 0 & 1 \end{bmatrix} \end{array}$$

$$V_n^1 \oplus V_n^3 \oplus V_n^4 = 0$$
$$V_n^1 \oplus V_n^2 \oplus V_n^5 = 0$$
$$V_n^2 \oplus V_n^3 \oplus V_n^6 = 0$$

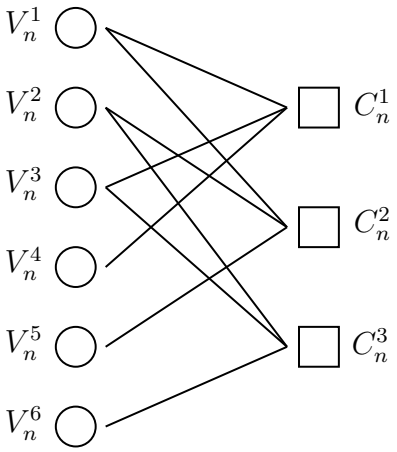

Figure 4.1: Tanner graph representation of an H matrix.

of a parity-check matrix along with its Tanner graph. The LDPC acronym refers to codes with a very low number of edges in its Tanner graph, i.e., with a very little number of ones in their parity-check matrix. LDPC codes are decoding efficient in combination with message passing algorithms (like the belief-propagation (BP), described in section 4.2).

CCSDS LDPC codes are quasi-cyclic codes. That means that the $\mathbf{H}$ matrix is composed by $Q \cdot Q$ sub-matrices, where $Q = k/4 = n/8$ if the code rate is 1/2; denoted with $\mathbf{I}_Q$ and $\mathbf{0}_Q$ respectively the identity and the null sub-matrices, an example of parity-check matrix for the LDPC (128, 64)

CCSDS code is described as

$$\mathbf{H}_{64,128} = \begin{bmatrix} \mathbf{I} \oplus \boldsymbol{\Phi}^{7} & \boldsymbol{\Phi}^{2} & \boldsymbol{\Phi}^{14} & \boldsymbol{\Phi}^{6} & \mathbf{0} & \boldsymbol{\Phi}^{0} & \boldsymbol{\Phi}^{13} & \mathbf{I} \\ \boldsymbol{\Phi}^{6} & \mathbf{I} \oplus \boldsymbol{\Phi}^{15} & \boldsymbol{\Phi}^{0} & \boldsymbol{\Phi}^{1} & \mathbf{I} & \mathbf{0} & \boldsymbol{\Phi}^{0} & \boldsymbol{\Phi}^{7} \\ \boldsymbol{\Phi}^{4} & \boldsymbol{\Phi}^{1} & \mathbf{I} \oplus \boldsymbol{\Phi}^{15} & \boldsymbol{\Phi}^{14} & \boldsymbol{\Phi}^{11} & \mathbf{I} & \mathbf{0} & \boldsymbol{\Phi}^{3} \\ \boldsymbol{\Phi}^{0} & \boldsymbol{\Phi}^{1} & \boldsymbol{\Phi}^{9} & \mathbf{I} \oplus \boldsymbol{\Phi}^{13} & \boldsymbol{\Phi}^{14} & \boldsymbol{\Phi}^{1} & \mathbf{I} & \mathbf{0} \end{bmatrix} \tag{4.2}$$

and its visual representation can be observed in Fig. 4.2. $\boldsymbol{\Phi}^{i}$ matrices are

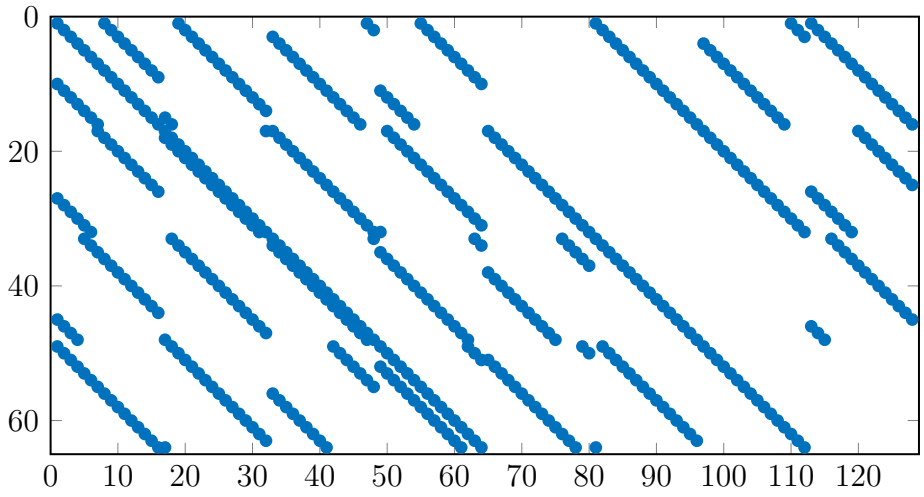

Figure 4.2: Visual representation of $\mathbf{H}_{64,128}$ LDPC code.

the i^{th} circular shift of $\mathbf{I}$. The $\oplus$ symbol represents the module 2 element-wise addition between two matrices. In Fig. 4.2 the blue dots represent the $h_{j,i} = 1$ elements.

The generator matrix can be obtained solving the equation $\mathbf{G} \cdot \mathbf{H}^{T} = \mathbf{0}_{k\times(n-k)}$. For the systematic hypothesis, however, the generator matrix is composed by the concatenation of an identity matrix $\mathbf{I}_k$, and a block-circulant matrix $\mathbf{W}_{k\times(n-k)}$. That matrix is specified by hexadecimal representation of the first rows of every sub-circulant matrices; the entire construction of every sub-matrices is obtained by the right circular shift of the own exadecimal description. For LDPC codes with 1/2 rate, the block circulant matrix $\mathbf{W}_{k\times(n-k)}$ is made by $4 \cdot 4$ square $Q \cdot Q$ sub-matrices $\mathbf{w}_{i,j}$.

This description of matrix $\mathbf{G}$ can be exploited to implement a very efficient encoding. For the generation of codeword $\mathbf{c}$, for example, the shift register adder accumulator (SRAA) method can be used. For ease of illustration, the 1/2 code rate case is described, but the method can be applied generally at every LDPC codes with different rate. Defined $\mathbf{u} = (\mathbf{u}_1, \mathbf{u}_2, \mathbf{u}_3, \mathbf{u}_4)$, where each $\mathbf{u}_i$ have length Q, the codeword $\mathbf{c}$ is represented by $\mathbf{c} = (\mathbf{u}_1, \mathbf{u}_2, \mathbf{u}_3, \mathbf{u}_4, \mathbf{p}_1, \mathbf{p}_2, \mathbf{p}_3, \mathbf{p}_4)$, where

$$\mathbf{p}_j = \mathbf{u}_1 \cdot \mathbf{w}_{1,j} + \mathbf{u}_2 \cdot \mathbf{w}_{2,j} + \mathbf{u}_3 \cdot \mathbf{w}_{3,j} + \mathbf{u}_4 \cdot \mathbf{w}_{4,j}. \tag{4.3}$$

Each $\mathbf{p}_j$ have length Q. In order to calculate the single $\mathbf{p}_j$, it is necessary to compute

$$\mathbf{u}_i \cdot \mathbf{w}_{i,j} = u_{(i-1)Q+1} \cdot \mathbf{g}_{i,j}^1 + u_{(i-1)Q+2} \cdot \mathbf{g}_{i,j}^2 + \cdots + u_{i \cdot Q} \cdot \mathbf{g}_{i,j}^Q \tag{4.4}$$

that is an efficient method to perform a vector-matrix product, knowing that the matrix is circulant. The l^{th} row of $\mathbf{w}_{i,j}$ is denoted with $\mathbf{g}_{i,j}^l$. With the SRAA implementation, equation (4.4) can be efficiently implemented in hardware (and also simulated in C++) using two shift register, Q AND logic, and Q XOR logic.

4.2 Decoder

The belief-propagation (BP) iterative algorithm is a bit-wise decoding method that calculates the a-posteriori likelihood ratio (LR) $L(c_i|\mathbf{y})$ for each variable node, starting from the a-priori information

$$L(c_i|y_i) = \frac{\mathbb{P}\{c_i = 0|y_i\}}{\mathbb{P}\{c_i = 1|y_i\}} \underset{\widehat{c}_i=0}{\overset{\widehat{c}_i=1}{\lessgtr}} 1 \tag{4.5}$$

which initially is the only available information.

The BP method consists in the mutual exchange of soft information be-

tween the VNs and the CNs. In the following, the log version of the decoding technique will be described. The algorithm is composed of four phases:

- initialization,

- horizontal step,

- vertical step,

- decision and check the stopping criterion,

the first one done only at the decoding start, while the others repeated cyclically until the stopping criterion is valid. The decoding terminates if a maximum number of iterations have been done, or if a valid codeword has been found. Horizontal and vertical denominations refer to the message passing steps, respectively from the CNs to the VNs and vice versa; the names recall that the CNs and the VNs are connected respectively to the rows and columns of the **H** matrix.

The initialization step consists in imposing, for every $j \in \mathcal{N}(i)$,

$$\overline{r}_i^j = \Lambda_i \tag{4.6}$$

where $\mathcal{N}(i)$ is the CNs connected with the i^{th} VN, $\overline{r}_i^j$ is the message from the VN i to the CN j, and Λ_i is the log version of the a-priori channel LR described in equation (4.5). Λ_i depends on the channel assumption.

In Fig. 4.3 is shown the visual representation of the horizontal step and of the vertical step (graph (a) and (b), respectively). Received the channel information, the CNs re-transmit to the neighbours VNs their own bit estimate. For every CNs j, the horizontal step message

$$\overline{m}_j^i = \prod_{k \in \mathcal{N}(j) \setminus \{i\}} \operatorname{sgn}\left(\overline{r}_k^j\right) \cdot \phi\left(\sum_{k \in \mathcal{N}(j) \setminus \{i\}} \phi\left(|\overline{r}_k^j|\right)\right) \tag{4.7}$$

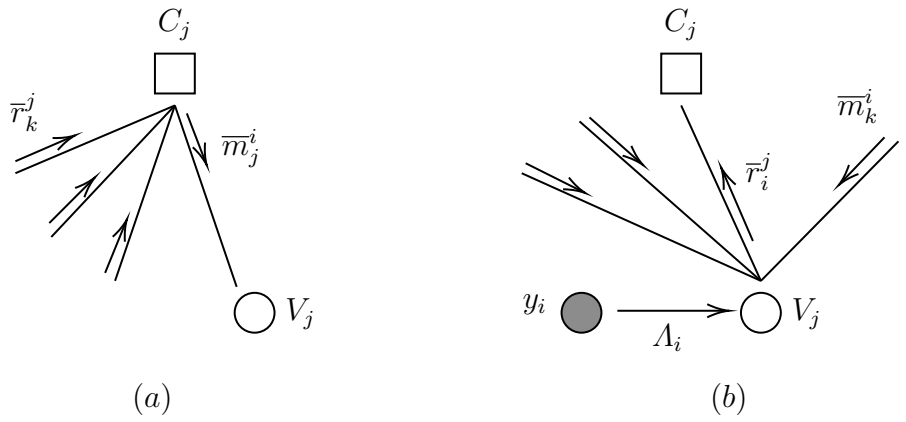

Figure 4.3: Horizontal step (a), and Vertical step (b).

is sent to the i^{th} VN. The message $\overline{m}_j^i$ includes all the information received at the j^{th} CN, except from the one the i^{th} VN itself sent previously. The function $\phi(\cdot)$ is described as

$$\phi(x) = \log\frac{e^x+1}{e^x-1} = -\log\left(\tanh\left(x/2\right)\right). \tag{4.8}$$

The vertical step consists of passing the VNs current bit estimates of their CNs neighbours. The message $\overline{r}_i^j$ is updated as

$$\overline{r}_i^j = \Lambda_i + \sum_{k\in\mathcal{N}(i)\setminus\{j\}} \overline{m}_k^i. \tag{4.9}$$

Message $\overline{r}_i^j$ does not include the previously received $\overline{m}_j^i$ information from the same CN.

Finally, the decision step is performed, calculating the LLRs from the information received, as

$$\Lambda^{\mathrm{VN}}(c_i|\Lambda_i, \mathbf{m}_i) = \Lambda_i + \sum_{k\in\mathcal{N}(i)} \overline{m}_k^i \underset{\widehat{c}_i=0}{\overset{\widehat{c}_i=1}{\lessgtr}} 0 \tag{4.10}$$

for every VNs. From this decisions, if the decoded $\widehat{\mathbf{c}}$ is a codeword the algorithm stops. Otherwise, another iteration starts from the second step.

4.3 Simulations and Results

The encoding and decoding algorithms previously described have been implemented in C++ language. Initially, the first version of the simulator supposes a BI-AWGN channel, in order to understand if the implementation would work correctly, because of the comparison with results obtained in a binary input Gaussian noise channel (from the *Encyclopedia of Sparse Graph Codes* by David J.C. MacKay). For this type of channel, and assuming an antipodal normalized mapping, the channel LLRs are

$$\Lambda_i = \frac{2}{\sigma^2}\, y_i \tag{4.11}$$

where σ^2 is the noise power of the Bi-AWGN channel.

Successively, an implementation of the 2-PPM channel has been done, in order to compare the performance graph of both the SCPPM and the LDPC methods. The PPM channel LLRs are described by the equation (1.3). Moreover, it is necessary to convert them into the LDPC Λ_i likelihoods [17].

The simulator also implements a reduced-complexity type of decoding, named Min-Sum (MS) decoding, and other two variations from this algorithm, named normalized Min-Sum (NMS) and offset Min-Sum (OMS). This three implementations differ from the basic one only for the horizontal step. The development of the MS decoder directly derives from equation (4.7): because of the $\phi(x)$ function, that assumes large values if the argument x is small, it is possible to approximate the horizontal step as

$$\overline{m}_j^i = \prod_{k \in \mathcal{N}(j)\setminus\{i\}} \operatorname{sgn}\left(\overline{r}_k^j\right) \cdot \min_{k \in \mathcal{N}(j)\setminus\{i\}} \left(\left|\overline{r}_k^j\right|\right). \tag{4.12}$$

A faster decoding is expected, along with worse performances than the basic iterative decoding ones. The NMS and the OMS algorithms are MS decoding variations, that should maintain its speed qualities, along with better performance. Both algorithms differ from the basic one for the horizontal step;

the NMS is described by

$$\overline{m}_j^i = \beta \cdot \prod_{k \in \mathcal{N}(j)\setminus\{i\}} \operatorname{sgn}\left(\overline{r}_k^j\right) \cdot \min_{k \in \mathcal{N}(j)\setminus\{j\}} \left(|\overline{r}_k^j|\right), \tag{4.13}$$

while the OMS by

$$\overline{m}_j^i = \prod_{k \in \mathcal{N}(j)\setminus\{i\}} \operatorname{sgn}\left(\overline{r}_k^j\right) \cdot \max\left(\min_{k \in \mathcal{N}(j)\setminus\{j\}} \left(|\overline{r}_k^j|\right) - \delta, 0\right) \tag{4.14}$$

Moreover, the C++ LDPC simulator implements two different type of message passing schedule. Message schedule means the order for which the information are exchanged by the VNs and the CNs. The algorithms until here described assume a Flooding schedule, also denoted as fully parallel mode. Messages $\overline{r}_i^j$ and $\overline{m}_j^i$ are computed in parallel, in their respectively steps; only when the calculation is over, all the nodes propagate in parallel all the information. The main advantage for this method is that the hardware implementation can be fully parallelized, while the main disadvantage is that, usually, the decoding algorithm needs more iteration than the other schedule in order to find a solution.
The second type of schedule is denominated Serial. For both the horizontal and vertical step the messages are computed and propagated serially; for example, the $j = 1$ CN will receive messages from its neighbour VNs; then it computes and propagates its $\overline{m}_1^i$, and finally the decision is performed. The process repeats serially for every CN j. This schedule does not admit the parallel hardware implementation, but seems to be faster in the codeword decoding.

In Fig. 4.4 are shown performance graphs derived from the 64,128 code described in equation (4.2) and in Fig. 4.2. The theoretical curve has been obtained from the *NEXTRACK TN1 - CONSOLIDATED TC C&S REQUIREMENTS* paper. The black curves have been achieved with the implemented C++ simulator, and represent the four different methods of the iterative decoding algorithm previously described. Fig. 4.4 refers to a BI-

AWGN channel, described with the channel LLRs of equation (4.11). The

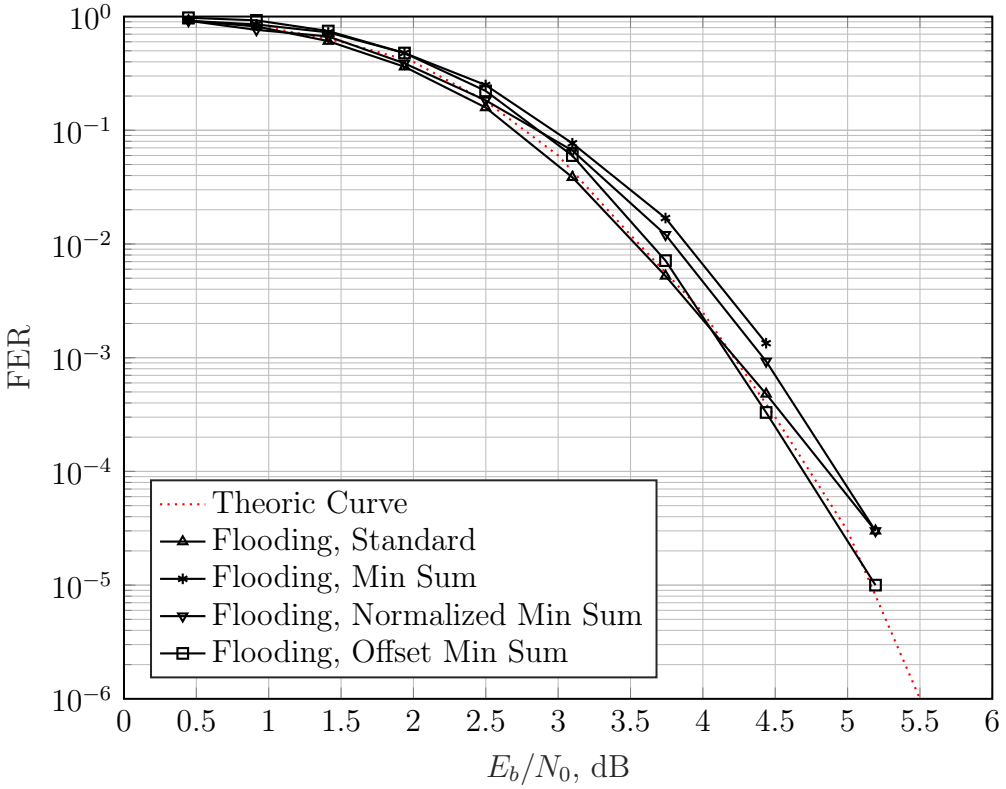

Figure 4.4: LDPC performance graphs, AWGN channel, (128,64) code.

four curves have been obtained with 100 decoding iterations each. Parameters β and δ in equations (4.13) and (4.14) have been imposed at 0.6 and 0.85, respectively. As expected, the standard BP method results the best type of decoding algorithm in regard to the FER quality. However, the other methods result faster, and the FER quality loss seems to be contained.

Fig 4.5, again, shows similar curves for the BI-AWGN channel, using the same code. However, it is shown a curve obtained with the serial schedule. It is clear that this schedule is faster in the frame decoding, because of the half number of iterations needed respect the 10 iterations of the flooding schedule curve. Moreover, the black curves show the FER quality improvement in relation to the number of decoding iterations.

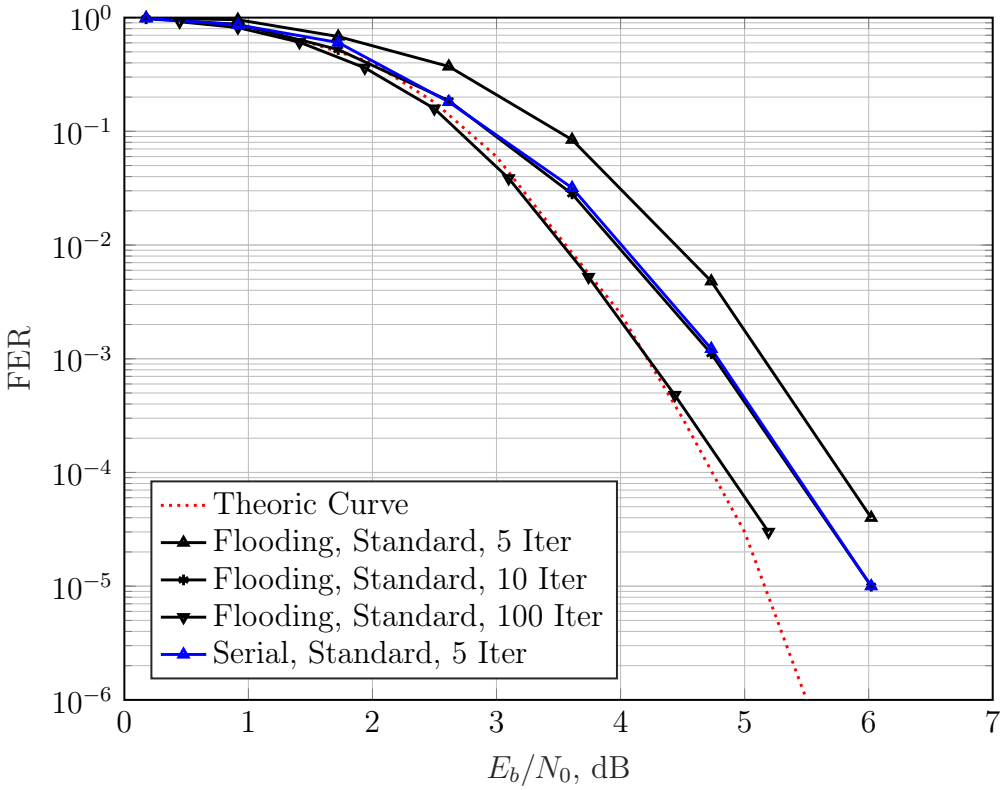

Figure 4.5: LDPC performance graphs, AWGN channel, (128,64) code. Comparison between serial and flooding method.

In Fig. 4.6 are shown two performance graphs of different length LDPC codes, obtained with considering the 2-PPM channel, and adding the puncturation to the C++ simulator. The two codes are a rate $1/2$, $n = 2048$, $k = 1024$, with the puncturation of the last 512 bits, and a rate $4/5$, $n = 1280$, $k = 1024$, with the puncturation of the last 128 bits. The algorithm used is the standard BP method, along with a flooding schedule; T_s is equal to 16 ns, and so $n_b = 0.2$ phe/slot. These graphs are comparable with the SCPPM ones, as the channel, and so the abscissa unit, are the same. As expected, the LDPC codes performance are worse than SCPPM codes. Compared with the $M = 4$, $R = 1/2$ SCPPM code, at FER $= 10^{-4}$, there is more than 3 dB of difference.

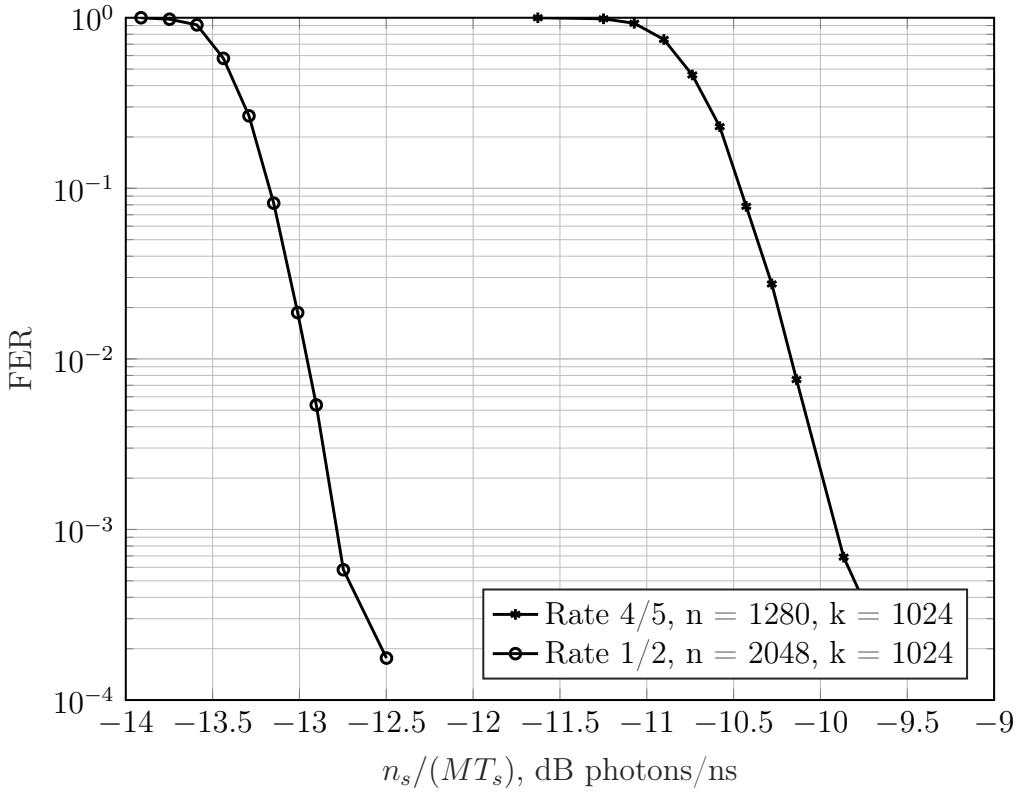

Figure 4.6: LDPC punctured codes in 2-PPM channel.

Chapter 5

Conclusions

In this thesis two possible implementations for a modulation and a demodulation system, along with the evaluation of some link budgets, have been studied. These considerations are done in a deep-space optical scenario, exploring the possibilities of future implementation of the described systems. This thesis also tried to examine the optical link of a 2-leg project; this aimed to understand if the 2-leg communication can take advantage of the optical segment, in regard to the link margin and the data rate achieved.

In chapter 1 some overall information about the optical channel, the global system losses, and the technologies used have been described. These information needs as fundamentals concepts for the successive chapters. SCPPM technique has been described in chapter 2, while the LDPC is shown in chapter 4. For both the sections, the description of the encoder and the iterative decoder have been described. Simulations and results derived from the C++ code developed have been reported and compared. Finally, in chapter 3 some considerations for possible future implementations of the methods have been described.

It has been found that, with the current technology constraints, optical communication between a relay orbiting around the Earth and Mars is possible. This thesis can also be taken as a basis study for future research

and applications. With the future development of the technologies, even the Neptune and Uranus links could be targeted.

List of Figures

Bibliography

[1] H. Hemmati, A. Biswas, and I. B. Djordjevic, "Deep-space optical communications: Future perspectives and applications," *Proceedings of the IEEE*, vol. 99, no. 11, pp. 2020–2039, 2011.

[2] B. Moision and J. Hamkins, "Coded modulation for the deep-space optical channel: serially concatenated pulse-position modulation," *IPN Progress Report*, vol. 42, no. 161, pp. 1–26, 2005.

[3] F. Zabini, B. Matuz, G. Liva, E. Paolini, and M. Chiani, "The PPM poisson channel: Finite-length bounds and code design," in *2014 8th International Symposium on Turbo Codes and Iterative Information Processing (ISTC)*. IEEE, 2014, pp. 193–197.

[4] B. Moision and J. Hamkins, "Deep-space optical communications downlink budget: modulation and coding," *IPN Progress Report*, vol. 42, no. 154, pp. 1–28, 2003.

[5] H. Hemmati, *Deep space optical communications*. John Wiley & Sons, 2006, vol. 11.

[6] A. Biswas, H. Hemmati, S. Piazzolla, B. Moision, K. Birnbaum, and K. Quirk, "Deep-space optical terminals (DOT) systems engineering," *IPN Progress Report*, vol. 42, p. 183, 2010.

[7] R. J. Daddato, K.-J. Schulz, and I. Zayer, "Deep space science downlinks via optical communication," in *2011 International Conference on Space Optical Systems and Applications (ICSOS)*. IEEE, 2011, pp. 8–13.

[8] H. Kaushal and G. Kaddoum, "Optical communication in space: Challenges and mitigation techniques," *IEEE communications surveys & tutorials*, vol. 19, no. 1, pp. 57–96, 2016.

[9] A. Biswas and S. Piazzolla, "Deep-space optical communications downlink budget from Mars: System parameters," *IPN Progress Report*, vol. 42, no. 154, pp. 0–1, 2003.

[10] N. K. Lyras, A. D. Panagopoulos, and P.-D. Arapoglou, "Deep-space optical communication link engineering: Sensitivity analysis," *IEEE Aerospace and Electronic Systems Magazine*, vol. 34, no. 11, pp. 8–19, 2019.

[11] C.-C. Chen and C. S. Gardner, "Impact of random pointing and tracking errors on the design of coherent and incoherent optical intersatellite communication links," *IEEE transactions on Communications*, vol. 37, no. 3, pp. 252–260, 1989.

[12] S. Guerrini, M. Chiani, M. Z. Win, and A. Conti, "Quantum pulse position modulation with photon-added coherent states," in *2019 IEEE Globecom Workshops (GC Wkshps)*. IEEE, 2019, pp. 1–5.

[13] V. Vilnrotter, A. Biswas, W. Farr, D. Fort, and E. Sigman, "Design and analysis of a first-generation optical pulse-position modulation receiver," *The Interplanetary Network Progress Report 42-148, October–December 2001*, pp. 1–20, 2002.

[14] G. Maral, M. Bousquet, and Z. Sun, *Satellite communications systems: systems, techniques and technology*. John Wiley & Sons, 2020.

[15] S. J. Orfanidis, "Electromagnetic waves and antennas, 2008," *Unpublished, available: http://www. ece. rutgers. edu/orfanidi/ewa*, 2004.

[16] L. Bahl, J. Cocke, F. Jelinek, and J. Raviv, "Optimal decoding of linear codes for minimizing symbol error rate (corresp.)," *IEEE Transactions on information theory*, vol. 20, no. 2, pp. 284–287, 1974.

[17] F. Xu, M. Khalighi, and S. Bourennane, "Pulse position modulation for FSO systems: Capacity and channel coding," in *2009 10th International Conference on Telecommunications*. IEEE, 2009, pp. 31–38.